A depth-averaged heart model for the inverse problem of cardiac electrophysiology

Emma Lagracie, Yves Bourgault, Yves Coudière, Lisl Weynans

A depth-averaged heart model for the inverse problem of cardiac electrophysiology

Emma Lagracie[1,2,3], Yves Bourgault[4], Yves Coudière[1,2,3], Lisl Weynans[1,2,3]

[1] Institut de Mathématiques de Bordeaux, Talence, France
[2] IHU Liryc, Talence, France
[3] Inria Bordeaux, Talence, France
[4] University of Ottawa, Ottawa, ON, Canada

Corresponding author: E. Lagracie, emma.lagracie@inria.fr

December 2024

Abstract

The inverse problem of cardiac electrophysiology is notoriously ill-posed, but is nonetheless extremely useful. In particular, it is difficult to reconstruct the transmembrane voltage in the volume of the heart, since an infinite dimensional space of transmembrane voltages can produce the same observation on the body surface. A widely used alternative is to consider only the outer surface of the heart, the epicardium, and solve a Cauchy problem for the Laplace equation in the torso domain. However, this approach only allows reconstruction of the extracellular potential on the epicardium, thus missing the information contained in the volume of the heart and in the transmembrane voltage.

We propose a new methodology for reconstructing activation maps from torso surface data, which incorporates information from the myocardial volume, while solving a surface problem on the heart. We formulate a static forward model, derived from the bidomain model, by averaging equations in the heart. The averaged equations are coupled with the usual Laplace equations in the surrounding domains. For solving the inverse problem, this «depth-averaged» forward model is used as a constraint in an optimal control problem that allows to recover depth-averaged transmembrane voltage and extracellular potential in the heart, corresponding to observations on the body surface. Activation maps are computed by post-processing the recovered signals in the heart. This method retains the ability to include the interactions between the heart, torso and blood cavities, while maintaining the simplicity of the usual inverse procedure. The inverse problem is solved with a simple linear system, using the Lagrangian formalism, and thus in a single iteration.

We emphasize on the post-processing techniques for recovering activation maps. We observe that using a threshold on the transmembrane voltage allows to recover smoother and more accurate activation maps than with a maximal deflection method on the extracellular potential.

Keywords Inverse problem, cardiac electrophysiology, activation times, asymptotic models

1 Introduction

Cardiac rhythm disorders is a leading cause of death around the globe [7, 24]. Sudden cardiac deaths account for between 20 and 25 % of total worldwide deaths [29]. However, the observation of arrythmias remains a challenge. Currently, identifying the sources of preexisting arrhythmias involve an invasive technique called the electroanatomical mapping (EAM). Clearly, this procedure carries inherent risks and requires prior knowledge of an existing disease. A promising approach called ECGi (electrocardiographic imaging) allows to reconstruct the heart's electrical activity, and notably its activation pattern, with a non-invasive technique [1]. The ECGi entails positioning a high density of electrodes on the patient's chest and solving a mathematical inverse problem known as the inverse problem of electrocardiography. However, the precise resolution of the inverse electrocardiography problem, and especially activation maps recovery, is still a work in progress [6].

The bidomain equations [30, 10, 18, 17] constitute the reference model for cardiac action potential, its propagation, and the generated electrical field. As the heart is surrounded by conductive media (blood, torso), the bidomain equations in the heart are coupled to potential equations in the torso and blood cavities. Considering a domain $\Omega = \Omega_B \cup \Omega_H \cup \Omega_T$ (blood cavities, heart and torso respectively - see Figure 1), we denote by $v : \Omega_H \to \mathbb{R}$ the transmembrane voltage and $u : \Omega \to \mathbb{R}$ the extracellular potential in the heart, and extracardiac potential in the blood or torso. In this article, we consider the non-dimensional following bidomain equation

$$\begin{cases} -\operatorname{div}(\sigma_i \nabla(u+v)) + \partial_t v + f(v,t) = 0 & \text{in } \Omega_H, \\ -\operatorname{div}((\sigma_e+\sigma_i)\nabla u) - \operatorname{div}(\sigma_i \nabla v) = 0 & \text{in } \Omega_H, \\ -\operatorname{div}(\sigma_{T/B}\nabla u) = 0 & \text{in } \Omega_T \ / \ \Omega_B, \\ [u] = 0 & \text{on } \bar{\Omega}_{T/B} \cap \bar{\Omega}_H, \\ \sigma_{T/B}\nabla u \cdot n = \sigma_e \nabla u \cdot n & \text{on } \bar{\Omega}_{T/B} \cap \bar{\Omega}_H, \\ \sigma_i \nabla(u+v)\cdot n = 0 & \text{on } \bar{\Omega}_{T/B} \cap \bar{\Omega}_H, \\ \sigma_T \nabla u \cdot n = 0 & \text{on } \partial\Omega. \end{cases} \tag{1}$$

The vector n denotes the normal pointing outward of Ω_H or of Ω. The parameter σ is the (scaled) conductivity tensor in the different mediums depending on the index, and f is the time-dependent ionic current. In practice the function f also depends on some ionic variables such as gating variables or ion concentration, that solve a system of ODEs. Concerning the inverse problem, those ODEs and the ionic model do not need to be specified. The potential u and transmembrane voltage v are searched as functions of $H^1(\Omega_H)$ and $H^1(\Omega)$ respectively. Note that the transmission conditions $[u] = 0$ and $\sigma_{T/B}\nabla u \cdot n = \sigma_e \nabla u \cdot n$ on $\bar{\Omega}_{T/B} \cap \bar{\Omega}_H$ derive directly from the condition $u \in H^1(\Omega)$. During the

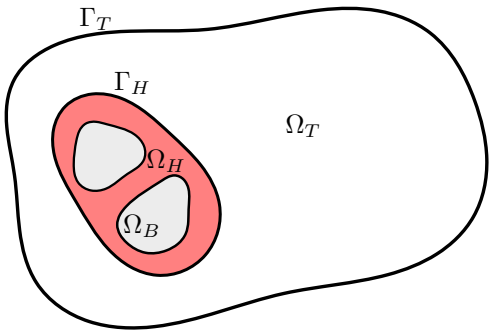

Figure 1: Schematic view of the domain $\Omega = \Omega_B \cup \Omega_H \cup \Omega_T$.

activation of the heart, the transmembrane voltage undergoes an action potential, the first phase of which is a rapid transition from a resting state to a plateau phase, known as depolarization. For a fixed $x \in \Omega_H$, the activation time is defined as the time of maximum temporal derivative of the transmembrane voltage. Activation occurs during depolarization. At a fixed x, the activation time is well understood, although it has several formal definitions. It can be characterized as the moment at which a threshold value is crossed, or equivalently, as the moment of minimum time derivative of the extracellular potential (maximal negative time derivative) [22, 1, 5]. The juxtaposition of the activation times of all the points in the heart constitutes the activation map, which is a valuable tool for cardiologists.

Activation maps can be reconstructed by solving the inverse problem of electrocardiography [25]. It consists in recovering the transmembrane voltage in the heart, or the extracellular potential, that produce a body surface potential which matches given measurements (data). Usually, the inverse problem is static, solved at several times independently, and relies on the electrostatic equilibrium equations contained in the bidomain model [1, 25]. Then the recovered signals are post-processed to compute activation maps. The inverse problem of electrocardiography is an ill-posed problem, making activation maps very difficult to recover. In addition, the reconstruction of activation maps from the reconstructed signals in the heart suffers from the formation of artificial lines of block [28, 5], which may falsely suggest a pathology. As the activation time can be detected on the extracellular potential via a minimal slope, the inverse problem is often limited to retrieving the extracellular potential u on the outer surface of the heart, the epicardium [1, 13, 25]. This problem, known as the "Potential-based inverse problem" [25] consists in finding u in the torso, and in particular its trace on the epicardium such that for a potential z_T measured on the surface

of the torso Γ_T (Γ_T coincides with the former $\partial\Omega$),

$$\begin{cases} -\operatorname{div}(\sigma_T \nabla u) = 0 & \text{in } \Omega_T \\ u = z_T & \text{on } \Gamma_T \\ \partial_n u = 0 & \text{on } \Gamma_T. \end{cases} \tag{2}$$

Note that in this formulation, the interactions with the heart do not appear, and that only volume Ω_T between the epicardium and the torso surface is taken into account. This is a ill-posed Cauchy problem, so the solution does not necessarily exist, although is unique when it does [2]. It is usually solved using a Tikhonov regularization.

Another method consists in recovering the transmembrane voltage v. This version has the great advantage of directly recovering the variable of interest for activation times. Some works aim to reconstruct the transmembrane voltage v in the thickness of the heart [11, 33, 23], while others seek only to retrieve this one on a surface, typically the epicardium or endorcardium or both [21]. As a matter of fact, the authors of [15, 14] justify the surface reconstruction by proving, under certain assumptions about the operators, that v can be reconstructed up to a constant on a surface, whereas throughout the myocardial domain (volume), an infinite dimensional distribution of transmembrane voltages can produce the same potential at the surface of the torso. Thus, regularization techniques and a priori solutions must be chosen wisely to reduce the space of solutions.

The inverse problem can also be directly formulated in terms of activation times. For instance, in [31, 26], the authors propose a predefined shape of transmembrane voltage v, that depends on a small number of parameters, including the activation time. Activation maps are then reconstructed through the resolution of a non-linear parameter identification problem. These parameter identification problems have a more constrained space of solution, and thus the effects of ill-conditioning are attenuated, however, they have the disadvantage of being non-linear, and therefore difficult to solve numerically. In addition, imposing a fixed shape for the action potential hampers the possibility of identifying a pathological signal.

Some researchers [19] have shown the ability to solve a complete bidomain-based inverse problem, using a given function f. However, this type of approach is very time-consuming and depends on extended knowledge about the ionic current f, which bears lots of uncertainty, especially in pathological cases.

In this article, we propose an intermediate mixed volume and surface inverse problem, that combines the advantages of reconstructing the transmembrane voltage on a surface, while incorporating some information on the interior of the myocardial wall via averaging.

We derive coupled equations between a surface-like heart and volumic torso and blood, by averaging the electrostatic equilibrium equation of the bidomain model in the cardiac wall thickness. It follows techniques used to derive fracture models in porous media [20, 16, 12]. The myocardial wall is assumed thin relatively to its extend, and we average the potential u and the voltage v along the wall thickness. As a consequence, the myocardial volume is replaced by an average surface. The model involves average potential $\bar{u}$ and voltage $\bar{v}$ defined on the surface. These functions are easier to identify than their volumic counterparts while retaining information on electrical transmission through the endocardial and epicardial layers.

This model is finally used as a constraint in an optimal control problem, in order to recover the average potential $\bar{u}$ and voltage $\bar{v}$ in the heart, from observations on the body surface. The cost function for the optimal control problem compares the data (electric field) on the torso boundary to the output of the model in a L^2 norm. This quadratic problem can be formulated as a linear system using the Lagrangian formalism. Therefore, it is solved in a single iteration as in [23]. We recover the average potential $\bar{u}$ and transmembrane voltage $\bar{v}$ in the heart, as well as u in both torso and blood volumes, with a formulation that naturally incorporates the couplings between the different domains. From the signals reconstructed over a discrete set of times, we recover tickness-averaged activation maps using two different methods, that we compare. In the light of our results, we suggest using a threshold on $\bar{v}$ to recover smoother and more accurate activation maps.

The paper is organized as follows: in Section 2, we develop the forward model, by averaging electrostatic equilibrium equation of the bidomain model in the thickness of the heart, in 2D geometries. Thus volumes become surfaces, and surfaces become curves. We verify its well-posedness, and implement the model in cartesian and polar geometries. We compare the depth-averaged model to the full 2D bidomain equations and pinpoint its limitations. In Section 3, we write an optimal control problem, based on the forward model, to recover the electrical potential and voltage in the heart from data available on the torso surface only. We prove the existence and uniqueness of the solution with regularization, and use a Lagrangian formulation for the implementation. In Section 4, we present some results, and test the

ability of the method to reconstruct activation maps. We also highlight the importance of reconstructing the transmembrane voltage for activation maps recovery.

2 A depth-averaged heart forward model

2.1 Derivation of the model

2.1.1 Assumptions

We place ourselves in a 2D geometry. Let $\Omega = \Omega_B \cup \Omega_H \cup \Omega_T$ be a bounded domain. Ω_B, Ω_H and Ω_T represent respectively the blood, heart and torso, and Ω_H separates the blood cavity from the torso. All boundaries are smooth. We denote by L the characteristic length of the heart. The thickness h of Ω_H is supposed to be small compared to the length L, $h \ll L$, and assumed constant. We denote by $\Gamma_T = \partial\Omega$ the torso surface. We also consider Γ_H a regular curve embedded in $\bar{\Omega}_H$. For instance, Γ_H may be given by the 0 level set of a C^1 signed distance function d: $\Gamma_H = \{x \in \Omega \text{ s.t. } d(x, \Gamma_H) = 0\}$. Generally, the heart domain closure $\bar{\Omega}_H$ encompasses the curve Γ_H such that, for $\lambda \in [0, 1]$, $\Omega_H = \{x \in \Omega \text{ s.t. } -\lambda h \leq d(x, \Gamma_H) \leq (1-\lambda)h\}$. Note that if $\lambda = 0$, Γ_H is located on the endocardium, while if $\lambda = 1$, Γ_H is located on the epicardium. We define the extended domains of blood $\tilde{\Omega}_B$ and torso $\tilde{\Omega}_T$ such that $\tilde{\Omega}_B = \{x \in \Omega \text{ s.t. } d(x, \Gamma_H) < 0\}$, and $\tilde{\Omega}_T = \{x \in \Omega \text{ s.t. } d(x, \Gamma_H) > 0\}$. Some example geometries of this form are presented in Figures 2, 3, 4.

We suppose that the fibers of the myocardium are parallel to Γ_H. This hypothesis is realistic, since up to a relatively small angle, the myocardial fibers are almost in the same plane as the boundaries of the heart (see [4]). The coordinate system associated to the heart determines a basis in which the conductivity tensors are diagonal. Indeed, in a cartesian geometry, the conductivity tensors write

$$\sigma_{i/e} = \begin{pmatrix} \sigma_{i/e,\ell} & 0 \\ 0 & \sigma_{i/e,p} \end{pmatrix}.$$

In a polar heart geometry, they are of the form

$$\sigma_{i/e} = P^T(\theta) \begin{pmatrix} \sigma_{i/e,p} & 0 \\ 0 & \sigma_{i/e,\ell} \end{pmatrix} P(\theta),$$

where P is the rotation matrix used to switch from the cartesian canonical basis to the (r, θ) polar basis. Note that the longitudinal direction is along x in the cartesian case and along θ in the polar case. The longitudinal and transverse conductivities $\sigma_\ell \geq \sigma_p > 0$ are taken constant. Outside of the heart, the conductivity tensors are isotropic, and thus reduce to scalars σ_T and σ_B. The indices i/e denote, respectively, the intracellular or extracellular medium. The conductivity σ_ℓ is the sum of $\sigma_{i,\ell} + \sigma_{e,\ell}$.

Note: This type of geometry does not include branching in the heart volume, so that the septum cannot be represented for example. The model would have to be adapted to deal with this type of geometry.

2.1.2 Model

We consider $\bar{u} : \Gamma_H \to \mathbb{R}$ an average potential in the heart, $u_T,\ u_B : \Omega_{T/B} \to \mathbb{R}$ the torso and blood electrical potentials, and $\bar{v} : \Gamma_H \to \mathbb{R}$ an average transmembrane voltage. Mathematically, we define $(\bar{u}, u_T, u_B)$ in $H^1(\Gamma_H) \times H^1(\tilde{\Omega}_T) \times H^1(\tilde{\Omega}_B)$ and $\bar{v}$ in $H^1(\Gamma_H)$ such that $\sigma_{i,\ell} h \frac{\partial^2}{\partial s^2} \bar{v}$ belongs to $L^2(\Gamma_H)$. We replace the bidomain equations (1) by the following static "depth-averaged " equations:

$$\begin{cases} \sigma_\ell h \dfrac{\partial^2}{\partial s^2} \bar{u} + \sigma_T \dfrac{\partial u_T}{\partial n}|_{\Gamma_H} + \sigma_B \dfrac{\partial u_B}{\partial n}|_{\Gamma_H} + \sigma_{i,\ell} h \dfrac{\partial^2}{\partial s^2} \bar{v} = 0 & \text{on } \Gamma_H, \\ \operatorname{div}(\sigma_T \nabla u_T) = 0 & \text{in } \tilde{\Omega}_T, \\ \operatorname{div}(\sigma_B \nabla u_B) = 0 & \text{in } \tilde{\Omega}_B, \end{cases} \tag{3}$$

coupled with the boundary conditions

$$\begin{cases} \sigma_T \partial_n u = 0 & \text{on } \Gamma_T, \\ \sigma_{e,p} \dfrac{u_T - \bar{u}}{h} = (1-\alpha) \sigma_T \partial_n u_T & \text{on } \Gamma_H, \\ \sigma_{e,p} \dfrac{u_B - \bar{u}}{h} = \alpha \sigma_B \partial_n u_B & \text{on } \Gamma_H. \end{cases} \tag{4}$$

The values $\bar{u}$ and $\bar{v}$ represent the in-depth averaged values of the potential u and transmembrane voltage v of the bidomain equations across the heart. The normal n is again directed from Γ_H to $\Omega_{B/T}$ or outward of Ω. The factor $0 < \alpha < 1$ is the barycentric coordinate of the average value location in the depth of the heart Ω_H. Note that α and λ may be different. For instance, in the cartesian geometry developed below, $\lambda = 1$, while in the polar geometry $\lambda = \frac{1}{2}$. For the numerical experiments, the value of α will be set at $\frac{1}{2}$ in both cases.

The Robin boundary conditions in (4) hide two assumptions: firstly, the average values $\bar{v}$ and $\bar{u}$ are located at the distance αh from the endocardium, and secondly, the potentials are assumed piecewise affine in the depth of the heart (see the section below on cartesian geometry). In the case $\alpha = 0$ or $\alpha = 1$, the Robin boundary conditions become Dirichlet conditions, changing the nature of the model. For the sake of simplicity, we will not address the case $\alpha = 0$ or $\alpha = 1$ in this paper.

The derivation of the "depth-averaged" model is justified in two particular cases, a cartesian geometry, and a polar geometry. By extension, we believe that it can be generally derived through a local map approach. This generalization will be studied in future work, in three dimensions.

Note: The model was also derived in the case of a variable heart thickness $h(x)$ in a cartesian geometry. Terms of order $h'(x)$ appear in the equations, however, if $\|h'\|$ is small respectively to h/L, the model remains identical at the leading order.

2.1.3 Example 1: Cartesian geometry

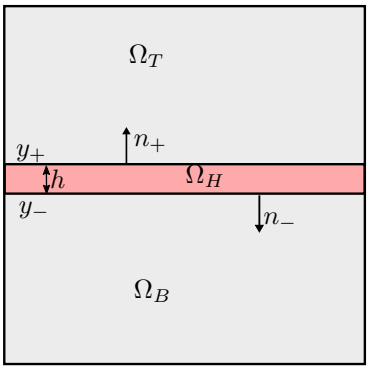

Figure 2: Cartesian geometry

We consider a rectangular geometry (Figure 2), where the blood and torso are separated by the heart. The heart is oriented along the x-axis, and the y-axis gives the transverse direction. The blood-heart and torso-heart interfaces are located, respectively, at $y = y_- = -\frac{h}{2}$ and at $y = y_+ = +\frac{h}{2}$. We suppose that $\sigma_B \nabla u \cdot n = 0$ on $\partial\Omega_B \setminus \partial\Omega_H$ and that $(\sigma_e + \sigma_i)\nabla u \cdot n = \sigma_i \nabla v \cdot n = 0$ on $\partial\Omega_H \setminus \partial\left(\Omega_T \cup \Omega_B\right)$.

Integrating the second equation of (1) in the heart along the y coordinate, and using the transmission conditions of the bidomain equations (1), we obtain

$$\begin{aligned} 0 =& \int_{y_-}^{y_+} \mathrm{div}((\sigma_i + \sigma_e)\nabla u)dy + \int_{y_-}^{y_+} \mathrm{div}(\sigma_i \nabla v) \\ =& \partial_x((\sigma_{i,\ell} + \sigma_{e,\ell})\partial_x(h\bar{u})) + \sigma_T \nabla u_T \cdot n_+ + \sigma_B \nabla u_B \cdot n_- + \partial_x(\sigma_{i,\ell}\partial_x(h\bar{v})) \quad \text{on } \Omega_H, \end{aligned} \tag{5}$$

where $\bar{v} = \frac{1}{h}\int_{y_-}^{y_+} v dy$ and $\bar{u} = \frac{1}{h}\int_{y_-}^{y_+} u dy$. These equations no longer depend on the depth of the heart, with the exception of the value of the fluxes, which are conditioned by the extracardiac potentials in the blood and torso. Since h/L is supposed small, we consider that the heart can be reduced to a line called Γ_H. We then extend the torso and blood domains to bridge the gap between $\partial\Omega_H$ and Γ_H, which yields the domains $\tilde{\Omega}_T$ and $\tilde{\Omega}_B$. We denote by Γ_- and Γ_+ the interface Γ_H approached, respectively, from the side of the blood or the torso. For a given depth-average transmembrane voltage $\bar{v}$, we then write a

system of equations involving $(\bar{u}, u_T, u_B) \in H^1(\Gamma_H) \times H^1(\Omega_T) \times H^1(\Omega_B)$, such that

$$\begin{cases} \partial_x((\sigma_{i,\ell} + \sigma_{e,\ell})\partial_x(h\bar{u})) + \sigma_T \nabla u_T \cdot n_+ + \sigma_B \nabla u_B \cdot n_- = -\partial_x(\sigma_{i,\ell}\partial_x(h\bar{v})) & \text{on } \Gamma_H, \\ \operatorname{div}(\sigma_T \nabla u_T) = 0 & \text{in } \tilde{\Omega}_T, \\ \operatorname{div}(\sigma_B \nabla u_B) = 0 & \text{in } \tilde{\Omega}_B, \\ u_T = \bar{u} & \text{on } \Gamma_+, \\ u_B = \bar{u} & \text{on } \Gamma_-. \end{cases} \tag{6}$$

However, the imposed Dirichlet conditions to link the values in and outside the heart are not satisfying, since we do not want to force u to be constant through the thickness of the heart. We will no longer consider them in the following. Instead, we choose to impose a Robin condition derived from the first-order approximation of the partial derivative in the y direction in Ω_H:

$$\frac{1}{\alpha h}(\bar{u} - u(y_-)) = -\partial_n u(y_-), \tag{7}$$

$$\frac{1}{(1-\alpha)h}(\bar{u} - u(y_+)) = -\partial_n u(y_+), \tag{8}$$

if we suppose that the value $\bar{u}$ is located at a distance αh from the endocardium surface ($0 < \alpha < 1$). Note that this finite difference type approximation of the derivative amounts to supposing that u is affine between the endocardium and an αh heart depth, and then between this αh depth and the epicardium. Thus u is assumed piecewise affine in the heart. Conversely, if u is assumed piecewise affine in depth in the heart and the value $\bar{u}$ located at a distance αh from the endocardium, we naturally recover the Robin conditions given. Using the continuity of the fluxes between the heart and the surrounding domains, and then mapping the actual heart boundaries to Γ_H, we recover the boundary conditions (4) presented in the previous section.

Note: The assumption of a piecewise affine potential u in the heart depth is not derived from the physiology of the heart, where u may have a more complex behavior. Considering that the heart is thin, it relies on a choice of using the minimal order approximation able to match the blood and torso fluxes on both sides of the heart.

Note: If there exists a bijective application from the actual interface $\bar{\Omega}_{B/T} \cap \bar{\Omega}_H$ to Γ_H, then we do not necessarily need to extend the blood and torso domains. We can establish a correspondance between the points of the $\bar{\Omega}_{B/T} \cap \bar{\Omega}_H$ boundaries and Γ_H, thus keeping the initial torso and blood boundaries positions. The system solved is then

$$\begin{cases} \sigma_\ell h \dfrac{\partial^2}{\partial x^2}\bar{u} + \sigma_T \dfrac{\partial u_T}{\partial n}|_{\bar{\Omega}_T \cap \bar{\Omega}_H} + \sigma_B \dfrac{\partial u_B}{\partial n}|_{\bar{\Omega}_B \cap \bar{\Omega}_H} + \sigma_{i,\ell} h \dfrac{\partial^2}{\partial x^2}\bar{v} = 0 & \Gamma_H, \\ \operatorname{div}(\sigma_T \nabla u_T) = 0 & \Omega_T, \\ \operatorname{div}(\sigma_B \nabla u_B) = 0 & \Omega_B, \end{cases} \tag{9}$$

coupled with

$$\begin{cases} \sigma_T \partial_n u = 0 & \text{on } \partial\Gamma_T, \\ \sigma_{ep}\dfrac{u_T - \bar{u}}{h} = (1-\alpha)\sigma_T \partial_n u_T & \text{on } \bar{\Omega}_T \cap \bar{\Omega}_H, \\ \sigma_{ep}\dfrac{u_B - \bar{u}}{h} = \alpha \sigma_B \partial_n u_B & \text{on } \bar{\Omega}_B \cap \bar{\Omega}_H. \end{cases} \tag{10}$$

2.1.4 Example 2: Polar geometry

If the heart geometry is an annulus, centered at the origin, we have

$$\Omega_H = \left\{ (r, \theta) \mid r \in (r_-, r_+) = (\bar{r} - \frac{h}{2}, \bar{r} + \frac{h}{2}), \theta \in [0, 2\pi] \right\}. \tag{11}$$

The shape of the torso is free of constraint. In polar coordinates and using the notation $\sigma = \sigma_i + \sigma_e$, the balance equation between u and v in the heart becomes

$$\frac{1}{r}\frac{\partial}{\partial r}\left(\sigma_p r \frac{\partial u}{\partial r}\right) + \frac{1}{r^2}\frac{\partial}{\partial \theta}\left(\sigma_\ell \frac{\partial u}{\partial \theta}\right) + \frac{1}{r}\frac{\partial}{\partial r}\left(\sigma_{ip} r \frac{\partial v}{\partial r}\right) + \frac{1}{r^2}\frac{\partial}{\partial \theta}\left(\sigma_{i\ell} \frac{\partial v}{\partial \theta}\right) = 0,$$

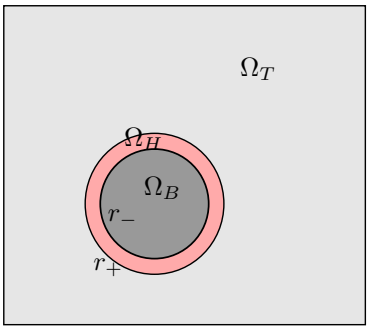

Figure 3: Polar geometry

that we multiply by r^2 and integrate across the heart thickness. The first two terms (in u) of the left-hand side yield:

$$\begin{aligned}&\int_{r_-}^{r_+}\left[r\frac{\partial}{\partial r}\left(\sigma_p r\frac{\partial u}{\partial r}\right)+\frac{\partial}{\partial\theta}\left(\sigma_\ell\frac{\partial u}{\partial\theta}\right)\right]dr\\ =&\sigma_\ell\frac{\partial^2}{\partial\theta^2}h\bar{u}+r_+^2\sigma_p\frac{\partial u}{\partial r}|_{r_+}-r_-^2\sigma_p\frac{\partial u}{\partial r}|_{r_-}-\sigma_p r_+u(r_+)+\sigma_p r_-u(r_-)+\sigma_p h\bar{u}\end{aligned}\tag{12}$$

We apply the hypothesis

$$\frac{1}{\alpha h}(\bar{u}-u(r_-))=-\partial_n u(r_-),\tag{13}$$

$$\frac{1}{(1-\alpha)h}(\bar{u}-u(r_+))=-\partial_n u(r_+),\tag{14}$$

analogous to (7) in the radial direction. Thus equality (12) becomes

$$\begin{aligned}&\sigma_\ell\frac{\partial^2}{\partial\theta^2}h\bar{u}+\left[\bar{r}+\frac{h}{2}\right]^2\sigma_p\frac{\partial u}{\partial r}|_{r_+}-\left[\bar{r}-\frac{h}{2}\right]^2\sigma_p\frac{\partial u}{\partial r}|_{r_-}-\sigma_p\left[\bar{r}+\frac{h}{2}\right]\bar{u}+\sigma_p\left[\bar{r}-\frac{h}{2}\right]\bar{u}\\ &-\sigma_p\left[\bar{r}+\frac{h}{2}\right](1-\alpha)h\partial_n u_{|\Gamma_+}+\sigma_p\left[\bar{r}-\frac{h}{2}\right]\alpha h\partial_n u_{|\Gamma_-}+\sigma_p h\bar{u}\\ =&\sigma_\ell\frac{\partial^2}{\partial\theta^2}h\bar{u}+\bar{r}^2\left[1+\alpha\frac{h}{\bar{r}}+\alpha\frac{1}{4}\frac{h^2}{\bar{r}^2}\right]\sigma_p\frac{\partial u}{\partial n}|_{\Gamma_+}+\bar{r}^2\left[1-(1-\alpha)\frac{h}{\bar{r}}+(1-\alpha)\frac{1}{4}\frac{h^2}{\bar{r}^2}\right]\sigma_p\frac{\partial u}{\partial n}|_{\Gamma_-}\end{aligned}\tag{15}$$

From now on, we define $A_1=\bar{r}^2\left[1+\alpha\frac{h}{\bar{r}}+\alpha\frac{1}{4}\frac{h^2}{\bar{r}^2}\right]$ and $A_2=\bar{r}^2\left[1-(1-\alpha)\frac{h}{\bar{r}}+(1-\alpha)\frac{1}{4}\frac{h^2}{\bar{r}^2}\right]$. Note that if $h/\bar{r}\ll 1$, A_1 and A_2 are at leading order equal to $\bar{r}^2$. Applying the same calculations on the terms in v and the transmission conditions from (1), the heart equation simplifies to

$$\sigma_\ell h\frac{\partial^2}{\partial\theta^2}\bar{u}+A_1\sigma_{ep}\frac{\partial u}{\partial n}|_{\Gamma_+}+A_2\sigma_{ep}\frac{\partial u}{\partial n}|_{\Gamma_-}+\sigma_{i,\ell}h\frac{\partial^2}{\partial\theta^2}\bar{v}=0\qquad\text{on }\Omega_H.\tag{16}$$

Again, we reduce that equation on a curve Γ_H using the hypothesis that $h/\bar{r}$ is small, and we extend the torso and blood domains to $\tilde{\Omega}_{B/T}$. Coupled with the usual Laplace equation in the blood cavity and torso, and the Robin boundary conditions, the complete model in the polar case writes

$$\begin{cases}\sigma_\ell h\dfrac{\partial^2}{\partial\theta^2}\bar{u}+A_1\sigma_T\dfrac{\partial u_T}{\partial n}|_\Gamma+A_2\sigma_B\dfrac{\partial u_B}{\partial n}|_\Gamma+\sigma_{i,\ell}h\dfrac{\partial^2}{\partial\theta^2}\bar{v}=0 & \text{on }\Gamma_H,\\ \operatorname{div}(\sigma_T\nabla u_T)=0 & \text{in }\tilde{\Omega}_T,\\ \operatorname{div}(\sigma_B\nabla u_B)=0 & \text{in }\tilde{\Omega}_B,\end{cases}\tag{17}$$

with the boundary conditions (4). On the curve Γ_H, the θ derivative also writes $\partial_\theta=\bar{r}\partial s$, with $s=\bar{r}\theta$. With that notation, we can uniformize the formulation at the order 0 to recover the more general formulation (3).

2.2 Variational formulation and properties of the problem

From now on, the domains $\tilde{\Omega}_B$ and $\tilde{\Omega}_T$ are assimilated to Ω_B and Ω_T: when considering the depth-averaged model, we will always deal with the extended domains of blood and torso.

2.2.1 Variational formulation

Let $\phi_T \in H^1(\Omega_T)$, $\phi_B \in H^1(\Omega_B)$, and $\bar{\phi} \in H^1(\Gamma_H)$ be three test functions. Multiplying the three equations of (3) by the three test functions, using Green's theorem and summing, we get

$$\begin{aligned}&\sigma_\ell h \int_{\Gamma_H} \frac{\partial}{\partial s}\bar{u}\frac{\partial}{\partial s}\bar{\phi} + \sigma_T \int_{\Omega_T} \nabla u_T \cdot \nabla \phi_T + \sigma_B \int_{\Omega_T} \nabla u_B \cdot \nabla \phi_B \\ &- \int_{\Gamma_H} \sigma_T \partial_n u_T(\bar{\phi} - \phi_T) - \int_{\Gamma_H} \sigma_B \partial_n u_B(\bar{\phi} - \phi_B) = \int_{\Gamma_H} \sigma_{i,\ell} h \frac{\partial \bar{v}^2}{\partial s^2}\bar{\phi},\end{aligned} \tag{18}$$

with n the normal directed towards the exterior of the heart. Let us denote $F = h\sigma_{i,\ell}\partial_{ss}\bar{v}$. Using the Robin boundary conditions (4) on the blood and torso sides, the variational formulation becomes:
Find $(\bar{u}, u_T, u_B)$ in $V = H^1(\Gamma_H) \times H^1(\Omega_T)/\mathbb{R} \times H^1(\Omega_B)$ such that

$$\begin{aligned}&\sigma_\ell h \int_{\Gamma_H} \frac{\partial}{\partial s}\bar{u}\frac{\partial}{\partial s}\bar{\phi} + \sigma_T \int_{\Omega_T} \nabla u_T \cdot \nabla \phi_T + \sigma_B \int_{\Omega_T} \nabla u_B \cdot \nabla \phi_B \\ &+ \frac{\sigma_{e,p}}{(1-\alpha)h} \int_{\Gamma_H} (\bar{u} - u_T)(\bar{\phi} - \phi_T) + \frac{\sigma_{e,p}}{\alpha h} \int_{\Gamma_H} (\bar{u} - u_B)(\bar{\phi} - \phi_B) = \int_{\Gamma_H} F\bar{\phi}, \quad \forall (\bar{\phi}, \phi_T, \phi_B) \in V.\end{aligned} \tag{19}$$

By a classical reasoning with test functions, the two equations (19) and (3) are proved to be equivalent.

2.2.2 Well-posedness

Compatibility condition Note that if the problem is formulated in terms of F, replacing the test functions $\bar{\phi}$, ϕ_T and ϕ_B by 1 in the variational formulation, the following compatibility condition must be satisfied

$$\int_{\Gamma_H} F = 0. \tag{20}$$

However, with $F = h\sigma_{i,\ell}\partial_{ss}\bar{v}$, and Γ_H a closed surface, the condition (20) is automatically true.

Theorem 1 (Well-posedness of the model (19)) *Given $F \in L^2(\Gamma_H)$ that verifies (20), there exists a unique solution $(\bar{u}, u_T, u_B)$ to the equation (19) in $V = H^1(\Gamma_H) \times H^1(\Omega_T)/\mathbb{R} \times H^1(\Omega_B)$. In addition, there exists a constant C such that*

$$\|(\bar{u}, u_T, u_B)\|_V \leq C\|F\|_{L^2(\Gamma_H)}.$$

Proof In order to obtain the uniqueness of the solution $(\bar{u}, u_T, u_B)$, we impose u_T to be a 0-mean function over Ω_T. Hence, the equation is posed in $V = H^1(\Gamma_H) \times H^1(\Omega_T)/\mathbb{R} \times H^1(\Omega_B)$, and we show that all hypotheses of Lax-Milgram's theorem are verified. We consider the product norm on V: $\|(\bar{u}, u_T, u_B)\|_V^2 = \|\bar{u}\|_{H^1(\Gamma_H)}^2 + \|u_T\|_{H^1(\Omega_T)}^2 + \|u_B\|_{H^1(\Omega_B)}^2$. We set

$$L\left(\bar{\phi}, \phi_T, \phi_B\right) = \int_{\Gamma_H} F\bar{\phi}\, ds$$

and

$$\begin{aligned}a\left((\bar{u}, u_T, u_B), (\bar{\phi}, \phi_T, \phi_B)\right) &= \sigma_\ell h \int_{\Gamma_H} \partial_s \bar{u}\partial_s\bar{\phi}\, ds + \int_{\Omega_T} \sigma_T \nabla u_T \nabla \phi_T + \int_{\Omega_B} \sigma_B \nabla u_B \nabla \phi_B \\ &+ \frac{\sigma_{e,p}}{(1-\alpha)h} \int_{\Gamma_H} (\bar{u} - u_T)(\bar{\phi} - \phi_T)\, d\Gamma + \frac{\sigma_{e,p}}{\alpha h} \int_{\Gamma_H} (\bar{u} - u_B)(\bar{\phi} - \phi_B)\, ds.\end{aligned}$$

First, let us recall some useful inequalities that will be used in the following.

1. **Jump inequality:** Using Young's inequality,

   $$g^2 = (g - h + h)^2 = (g-h)^2 + 2(g-h)h + h^2 \leq 2((g-h)^2 + h^2).$$

   And so $(g-h)^2 \geq \frac{1}{2}g^2 - h^2$.

2. **Poincaré-Friedrich:** For Ω a domain (lipschitz bounded connected open), there exists $C_{\mathrm{PF}} > 0$ such that

   $$C_{PF}\|\phi\|_{H^1(\Omega)}^2 \leqslant \int_\Omega |\nabla\phi|^2 + \left(\int_{\partial\Omega} \phi(x)\right)^2 \leqslant \int_\Omega |\nabla\phi|^2 + |\partial\Omega| \int_{\partial\Omega} \phi^2,\ \forall \phi \in H^1(\Omega).$$

3. **Poincaré-Wirtinger:** For Ω a domain, there exists $C_{PW} > 0$ such that for all $u \in H^1(\Omega)$,

$$\left\| u - \frac{1}{|\Omega|}\int_\Omega u \right\|^2_{L^2(\Omega)} \leq C_{PW}\|\nabla u\|^2_{L^2(\Omega)}.$$

4. **Trace continuity:** For Ω a domain, there exists C_{Tr} such that for $u \in H^1(\Omega)$, $\|u\|_{L^2(\partial\Omega)} \leq C_{Tr}\|u\|_{H^1(\Omega)}$.

The right-hand side of (19) is obviously linear, and continuous:

$$\left|L\left(\bar\phi, \phi_T, \phi_B\right)\right| = \left|\int_{\Gamma_H} F\bar\phi\right| \leq \|F\|_{L^2(\Gamma_H)}\|\bar\phi\|_{L^2(\Gamma_H)} \leq \|F\|_{L^2(\Gamma_H)}\|\left(\bar\phi, \phi_T, \phi_B\right)\|_V.$$

We also have the inequality below, where $C > 0$ denotes any constant independent from $(\bar u, u_T, u_B)$

$$\begin{aligned}\left|a\left((\bar u, u_T, u_B), (\bar\phi, \phi_T, \phi_B)\right)\right| &\leq C\|\bar u\|_{H^1(\Gamma_H)}\|\bar\phi\|_{H^1(\Gamma_H)} + C\|u_T\|_{H^1(\Omega_T)}\|\phi_T\|_{H^1(\Omega_T)} + C\|u_B\|_{H^1(\Omega_B)}\|\phi_B\|_{H^1(\Omega_B)}\\ &+ C\|\bar u - u_T\|_{L^2(\Gamma_H)}\|\bar\phi - \phi_T\|_{L^2(\Gamma_H)} + C\|\bar u - u_B\|_{L^2(\Gamma_H)}\|\bar\phi - \phi_B\|_{L^2(\Gamma_H)}\\ &\leq C\|\left(\bar u, u_T, u_B\right)\|_V\|\left(\bar\phi, \phi_T, \phi_B\right)\|_V,\end{aligned}$$

using the triangular inequality on $\|\bar u - u_{T/B}\|_{L^2(\Gamma_H)}$ and then the trace continuity. Thus a is continuous on V. Applying the jump inequality to $\left|\bar u - u_{B/T}\right|^2$, we get

$$\begin{aligned}a\left((\bar u, u_T, u_B), (\bar u, u_T, u_B)\right) &= \sigma_\ell h\int_{\Gamma_H}|\partial_s\bar u|^2 + \int_{\Omega_T}\sigma_T\left|\nabla u_T\right|^2 + \int_{\Omega_B}\sigma_B\left|\nabla u_B\right|^2\\ &+ \frac{\sigma_{e,p}}{(1-\alpha)h}\int_{\Gamma_H}|\bar u - u_T|^2 + \frac{\sigma_{e,p}}{\alpha h}\int_{\Gamma_H}|\bar u - u_B|^2\\ &\geq \sigma_\ell h\int_{\Gamma_H}|\partial_s\bar u|^2 + \int_{\Omega_T}\sigma_T\left|\nabla u_T\right|^2 + \int_{\Omega_B}\sigma_B\left|\nabla u_B\right|^2\\ &+ C_3\int_{\Gamma_H}|\bar u - u_T|^2 + C_4\int_{\Gamma_H}|\bar u - u_B|^2\\ &\geq \sigma_\ell h\|\partial_s\bar u\|^2_{L^2(\Gamma_H)} + \sigma_T\|\nabla u_T\|^2_{L^2(\Omega_T)} + \sigma_B\|\nabla u_B\|^2_{L^2(\Omega_B)}\\ &+ \frac{C_3}{2}\|\bar u\|^2_{L^2(\Gamma_H)} - \underbrace{C_3\|u_T\|^2_{L^2(\Gamma_H)}}_{\geq -C_3C_{Tr}\|u_T\|^2_{H^1(\Omega_T)}} + \frac{C_4}{2}\|u_B\|^2_{L^2(\Gamma_H)} - C_4\|\bar u\|^2_{L^2(\Gamma_H)},\end{aligned}$$

where $\frac{\sigma_{e,p}}{(1-\alpha)h} \geq C_3 > 0$, $\frac{\sigma_{e,p}}{\alpha h} \geq C_4 > 0$. Using the Poincaré-Friedrich inequality and regrouping some terms, we finally get

$$\begin{aligned}a\left((\bar u, u_T, u_B), (\bar u, u_T, u_B)\right) \geq \min\left(\sigma_\ell h, \frac{C_3}{2}\right)\|\bar u\|^2_{H^1(\Gamma_H)} &- C_4\|\bar u\|^2_{H^1(\Gamma_H)}\\ + \frac{\sigma_T}{2}\min\left(1, C_{PW}^{-1}\right)\|u_T\|^2_{H^1(\Omega_T)} &- C_3C_{Tr}\|u_T\|^2_{H^1(\Omega_T)}\\ + C_{PF}\min\left(\sigma_B, \frac{C_4}{2}|\Gamma_H|^{-1}\right)\|u_B\|^2_{H^1(\Omega_B)}&\end{aligned} \tag{21}$$

The constants $C_3 > 0$ and $C_4 > 0$ initially appear in front of positive terms. They can therefore be chosen to be arbitrarily small. We choose $C_3 = \frac{1}{2}\frac{1}{C_{Tr}}\frac{\sigma_T}{2}\min\left(1, C_{PW}^{-1}\right)$, and $C_4 = \frac{1}{2}\min\left(\sigma_\ell h, \frac{C_3}{2}\right)$. Denoting

$$c = \min\left(C_4, C_{PF}\min\left(\sigma_B, \frac{C_4}{2}|\Gamma_H|^{-1}\right)\right),$$

$$a\left((\bar u, u_T, u_B), (\bar u, u_T, u_B)\right) \geq c\left[\|\bar u\|^2_{H^1(\Gamma_H)} + \|u_T\|^2_{H^1(\Omega_T)} + \|u_B\|^2_{H^1(\Omega_B)}\right], \tag{22}$$

and so $a(.,.)$ is coercive.

2.3 Numerical strategy and validation

We compare numerically the depth-averaged model (3) with the bidomain model (1) in cartesian and polar geometries.

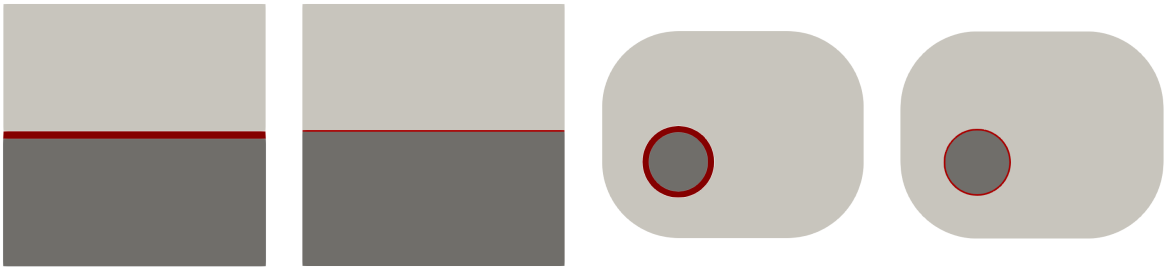

(a) (b) (c) (d)

Figure 4: Geometries used for the numerical simulations: (a) Cartesian bidomain model, (b) Cartesian depth-averaged model, (c) Polar bidomain model, (d) Polar depth-averaged model.

2.3.1 Method

Geometries considered The geometries used for the numerical validation of the model are presented in Figure 4. The cartesian geometry is the square $[-1,1]\times[-1,1]$. We use a mesh size of 0.01. Concerning the polar geometry, the torso is approximately a 3 by 2 unit rectangle, with round corners, and the heart is a circle of medium radius 0.3 and width $h = 0.06$. The relative size of the human heart with the torso is approximately respected. The mesh size is 0.02. Several possibilities exist for placing the heart layer Γ_H in the original bidomain geometry (it can be expressed in terms of λ introduced in section 2.1.1). We chose to place the layer on the epicardium ($\lambda = 1$) for the cartesian geometry and halfway between the epicardium and the endocardium ($\lambda = 0.5$) for the polar geometry. The void originally occupied by the heart is filled with blood mesh or torso mesh, to define the extended domains $\tilde{\Omega}_{B/T}$. Our simulations showed that the placement of the layer does not have a significant impact on the solutions.

Bidomain model parameters and scenarios The bidomain simulations are performed with anisotropic conductivity tensors in the heart: $\sigma_{i,\ell} = 1.741$, $\sigma_{i,p} = 0.1934$, $\sigma_{e,\ell} = 3.906$, $\sigma_{e,p} = 1.970$, and isotropic in the torso and blood: $\sigma_T = \sigma_B = 2$. The eigenvalues in the heart were taken from [27]. The ionic model chosen is the Mitchell-Shaeffer model [22], with parameter values given in the paper. We designed several scenarios of activation in the heart corresponding to different number and location of initial excitation sites. An excitation site is a localized current source applied to the heart and characterized by its application point x_s, radius r_s and intensity. The stimulations are of constant intensity 1 in $\{x \in \Omega_H \mid |x_s - x| < r_s\}$, and decrease smoothly (cubic function) to 0 in $\{x \in \Omega_H \mid |x_s - x| < r_s + e\}$, with Mesh Size $< e < r_s$. For the cartesian geometry, the propagation of the activation was initiated in two stimulation sites located at coordinates $(-0.2, 0)$ and $(0, 0)$. In the polar geometry, four pacing

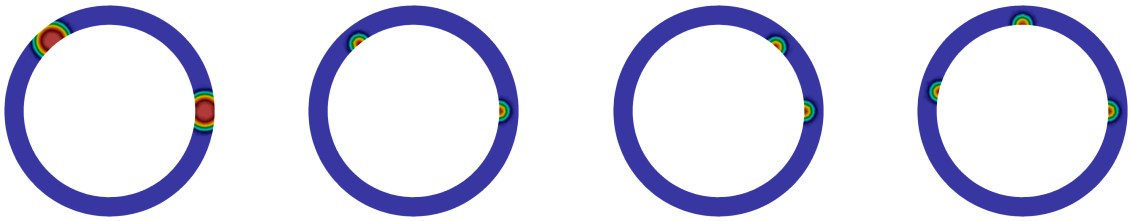

(a) Pacing protocol 1. (b) Pacing protocol 2. (c) Pacing protocol 3. (d) Pacing protocol 4.

Figure 5: Pacing protocols 1, 2, 3 and 4 from left to right used in the polar geometry.

protocols for the bidomain were designed, see Figure 5. In protocol 1, we initiate the propagation of the action potential at angles $\theta = 0$ and $\theta = 3\pi/4$, in the middle of the myocardium wall. In protocol 2, 3 and 4, we stimulate on the endocardium, as it is the case in a regular sinusal rythm. In the protocol 2, the angles of stimulation are the same as in protocol 1, but on the endocardium. In stimulation protocol 3, the points of stimulation are brought together at $\theta = 0$ and $\pi/4$. The last protocol presents three stimulation points, located in $\theta = 0$, $\pi/2$ and 0.9π.

Numerical methods On the one hand, the depth-averaged problem was solved using P^1 Lagrange finite elements. The heart layer Γ_H was approximated by a polygon. On the heart, the mass matrix was computed exactly with a Simpson quadrature. On the other hand, the bidomain equations were implemented with the Discrete Duality Finite Volume (DDFV) scheme in space, and the Semi-implicit second order Backward Differentiation Formula (SBDF2) temporal scheme [8] with a time step of 0.1 ms for the ionic Mitchell-Shaeffer model.

Discrete system for the depth-averaged model For the discrete system, we consider the unknown vector

$$X = \left[U_B,\ U_T,\ \bar{U}\right]^T = \left[U_{B|\mathring{\Omega}_B},\ U_{B|\Gamma_H},\ U_{T|\Gamma_H},\ U_{T|\mathring{\Omega}_T},\ U_{T|\Gamma_T},\ \bar{U}\right]^T,$$

where the components of the vectors $U_{B/T}$ (resp. $\bar{U}$) are the values of the functions $u_{B/T}$ (resp. $\bar{u}$) at the nodes of the mesh. We denote by $(\varphi_i)_i$ the P^1 Lagrange basis functions. The mass and stiffness matrices on Γ_H, namely M_{Γ_H} and K_{Γ_H} write

$$[M_{\Gamma_H}]_{i,j} = \left(\int_{\Gamma_H} \varphi_i\varphi_j\, ds\right), \quad [K_{\Gamma_H}]_{i,j} = \left(\int_{\Gamma_H} \partial_s\varphi_i\partial_s\varphi_j\, ds\right).$$

In the blood and torso domains, the mass and stiffness matrix $\mathbb{M}_{B/T}$ and $\mathbb{K}_{B/T}$ write

$$[\mathbb{M}_{B/T}]_{i,j} = \left(\int_{B/T} \varphi_i\varphi_j\, ds\right), \quad [\mathbb{K}_{B/T}]_{i,j} = \left(\int_{B/T} \nabla\varphi_i\cdot\nabla\varphi_j\, ds\right).$$

The projection matrix from the finite element space on Ω_B (resp. Ω_T) to the finite element space on Γ_H are called P_H^B, and P_H^T. We also denote $C_1 = \frac{\sigma_{e,p}}{(1-\alpha)h}$ and $C_2 = \frac{\sigma_{e,p}}{\alpha h}$. Then, in the finite-dimensional space generated by the P^1 Lagrange basis, the equation (19) writes

$$\mathbb{A}\begin{pmatrix} U_B \\ U_T \\ \bar{U}\end{pmatrix} = \begin{pmatrix} 0 \\ 0 \\ M_{\Gamma_H}F\end{pmatrix}.$$

In the case of a closed surface Γ_H, $M_{\Gamma_H}F = -\sigma_{i,l}hK_{\Gamma_H}\bar{V}$. The matrix of the system is given by

$$\mathbb{A} = \begin{pmatrix} A_2\sigma_B\mathbb{K}_B + C_2(P_H^B)^t M_{\Gamma_H}P_H^B & 0 & -C_2(P_H^B)^t M_{\Gamma_H} \\ 0 & A_1\sigma_T\mathbb{K}_T + C_1(P_H^T)^t M_{\Gamma_H}P_H^T & -C_1(P_H^T)^t M_{\Gamma_H} \\ -C_2 M_{\Gamma_H}P_H^B & -C_1 M_{\Gamma_H}P_H^T & \sigma_\ell h K_{\Gamma_H} + (C_1+C_2)M_{\Gamma_H}\end{pmatrix}.$$

Resolution of the linear system To ensure the invertibility of the system, we use the usual technique of adding a scaled lumped mass matrix on the Ω_T domain in the equation. The system solved in practice is

$$\mathbb{A} + \varepsilon_C\begin{pmatrix} 0 & 0 & 0 \\ 0 & \sigma_T\mathbb{M}_T & 0 \\ 0 & 0 & 0\end{pmatrix}\begin{pmatrix} U_B \\ U_T \\ \bar{U}\end{pmatrix} = \begin{pmatrix} 0 \\ 0 \\ -\sigma_{i,l}hK_{\Gamma_H}\bar{V}\end{pmatrix}.$$

The parameter ε_C is taken as 10^{-14}. Then, the constant of the solution is adjusted to impose $\int_{\Omega_T} u_T = 0$. We used a direct LU solver from the `scipy.sparse` Python library.

Averaged values of reference The reference data $\bar{u}$ and $\bar{v}$ are obtained by averaging the bidomain potential u and voltage v over the heart thickness.

2.3.2 Numerical validation

One must keep in mind that the solution of the bidomain and the solution of the depth-averaged model can differ by a constant. Indeed, in the bidomain model, the constant is fixed such that $\int_{\Omega_H\cup\Omega_B\cup\Omega_T} u = 0$, while in the averaged model, only u_T is of 0-mean: $\int_{\Omega_T} u_T = 0$. Our numerical simulations showed no significant differences between the solutions of the depth-averaged model with different values of the parameter α. Thus, in all the following tests, α is fixed at $\alpha = 0.5$.

Some examples of numerical solutions are presented in Figure 6 for the cartesian geometry, and in Figure 7 for a polar geometry. In the cartesian geometry with transmural pacing (protocol 1), the

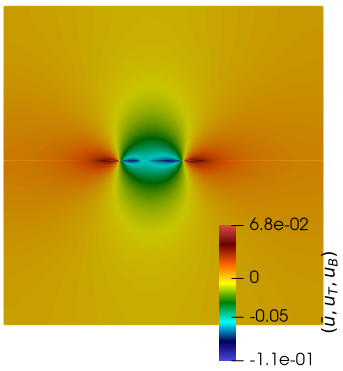

(a) $\bar{u}$, u_T, u_B solution of the depth-averaged model. $t = 6$ ms.

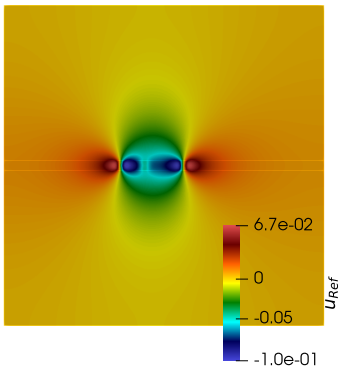

(b) Potential u from the bidomain model. $t = 6$ ms.

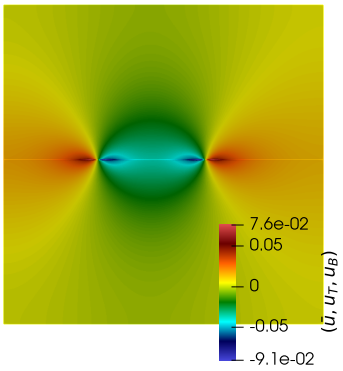

(c) $\bar{u}$, u_T, u_B solution of the depth-averaged model. $t = 14$ ms.

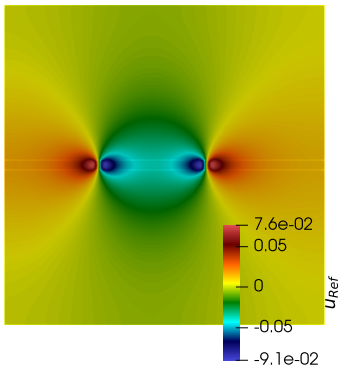

(d) Potential u from the bidomain model. $t = 14$ ms.

Figure 6: Solution of the depth-averaged model (left) compared to the bidomain reference (right) in a cartesian geometry at two different times.

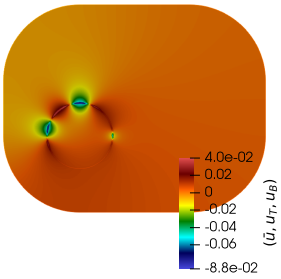

(a) $(\bar{u}, u_T, u_B)$ solution of the depth-averaged model.

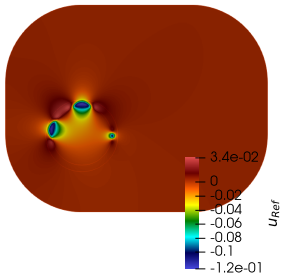

(b) Potential u from the bidomain model.

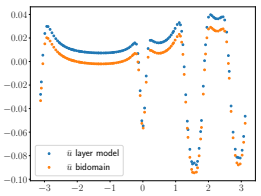

(c) $\bar{u}$ of reference (orange) and depth-averaged model (blue) on Γ_H.

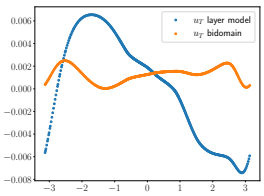

(d) u_T of reference (orange) and depth-averaged model (blue) on the torso surface.

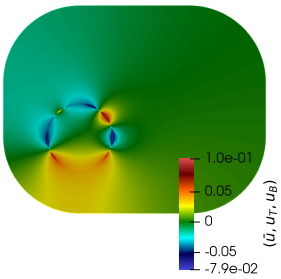

(e) $(\bar{u}, u_T, u_B)$ solution of the depth-averaged model.

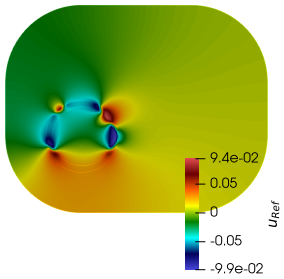

(f) Potential u from the bidomain model.

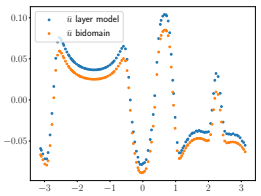

(g) $\bar{u}$ of reference (orange) and depth-averaged model (blue) on Γ_H.

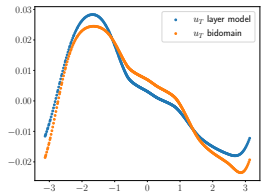

(h) u_T of reference (orange) and depth-averaged model (blue) on the torso surface.

Figure 7: Solutions of the averaged and bidomain models on heart and torso layers in the case of pacing protocol 4. The upper subfigures (a), (b), (c), (d) present the solutions at time $t = 6$ ms, and the bottom subfigures (e), (f), (g), (h) show the solutions at times $t = 13$ ms. At $t = 6$ ms, the activation has not reached the epicardium yet while at $t = 13$ ms, the activation has already reached the epicardium.

potential obtained with the depth-averaged model is qualitatively very similar to the bidomain reference potential. Moreover, the amplitude of the solution $(\bar{u}, u_T, u_B)$ is identical to the amplitude of the solution of the bidomain u_{Ref} taken at the same time instant. Indeed, for a transmural pacing, there is a symmetry between the epicardium and endocardium potential and voltages. In that case, our forward model represents accurately the potentials in the torso and on the heart.

Concerning the more realistic polar geometry (Figure 7), the behaviour of the solution of the depth-averaged model compared to the bidomain reference strongly depends on the initial stimulation protocol. Qualitatively, when the activation has reached the epicardium (subfigures (7e), (7f), (7g), (7h), taken at $t = 13$ ms), the shape of the potentials u_T and $\bar{u}$ are preserved. They are very similar to the bidomain ones despite some very localized discrepancy. However, for an endocardial pacing (which would be the case in a regular sinusal rythm), the activation wave does not reach immediatly the epicardium. Before it attains the epicardium, the activation is very hard to observe on the body surface. The strong variations of potential are confined inside the heart and do not propagate to the torso, thus generating only residual signal on the torso surface. In that case, our model strongly differs in the torso from the bidomain solution, producing body surface potential that have a larger amplitude than the true signal (see the subfigures (7a), (7b), (7c), (7d) taken at $t = 6$ ms). In other words, the depth-averaged model creates artificial transmission of information from the myocardial layer to the torso before the epicardial breakthrough. Still, we observed that our model is sufficiently accurate after the epicardial breakthrough to attempt using it for cardiac source recovery. However, as it is already the case with the original bidomain system, we do not expect to identify precisely what happens inside the heart before the activation signal reaches the epicardium.

3 Inverse problem

In this section, we formulate an optimal control problem to find a solution $(\bar{u}, u_B, u_T)$ of the depth-averaged model (19) with the right-hand-side F as a control, which matches some torso surface potential data. If such a control F can be found, then the average transmembrane voltage $\bar{v}$ can be recovered up to a constant on the layer of the heart Γ_H.

3.1 Presentation of the optimal control problem

We call z_T the body surface potential map (BSPM) data available, where for the sake of our analysis, z_T is a function from Γ_T to $\mathbb{R}$. We consider $F = h\sigma_{i,\ell}\partial_{ss}\bar{v}$ the electrical sources in the heart, and $U[F] = (\bar{u}, u_T, u_B)$ the extracellular potential generated by F in the depth-averaged model (19). We define the functional

$$J(U[F], F) = \frac{1}{2}\int_{\Gamma_T} |u_T - z_T|^2 + \frac{\varepsilon}{2}|F|^2_{H^1(\Gamma_H)}.$$

The semi-norm $|.|_{H^1(\Gamma_H)}$ is defined by $|g|_{H^1(\Gamma_H)} = \|\nabla g\|_{L^2(\Gamma_H)}$. In this formulation, we search for the optimal control F that minimizes the functional J. The source F is in $H^1(\Gamma_H)/\mathbb{R}$ (functions of $H^1(\Gamma_H)$ with 0-mean over Γ_H) to satisfy the compatibility condition (20). The first term of J ensures that the minimizing control matches the data z_T. The second term is the first-order Tikhonov regularization of the inverse problem, necessary for the well-posedness of the problem. A quadratic norm for the regularization term allows to obtain linear conditions of optimality for the optimal control problem. Moreover, we classically regularize on the derivative of the control to constrain its variations. This is why we have chosen the H^1 semi-norm.

Theorem 2 (Existence and uniqueness of an optimal control for J) *There exists a unique control F that minimizes J in the constrained space of solutions of the depth-averaged forward model.*

The proof is detailed in the following subsection. There is one technical point in the sense that the constant of the potential $U[F]$ needs to be adjusted to match the data. In the proof, we formulate the optimal control problem in terms of couple (U, F), and search U in a constrained affine space, depending on F. The constant of the potential is then naturally adjusted in the minimization process.

3.2 Proof of Theorem 2.

3.2.1 Spaces for the control F and potential U

We consider J as a function of (U, F). The potential U, solution of (19) in $H^1(\Gamma_H) \times H^1(\Omega_T) \times H^1(\Omega_B)$, lives in the constrained affine space $AF + \mathbb{R}$, where A is the continuous bijective operator associated to the state equation (19) (variational formulation of the depth-averaged model, see well-posedness of the forward problem). If we denote $U_0 = AF$ the unique solution of (19) in the space $V = H^1(\Gamma_H) \times H^1(\Omega_T)/\mathbb{R} \times H^1(\Omega_B)$, then U would write $U = U_0 + C$, $C \in \mathbb{R}$. Notice that the observation $u_{T|\Gamma_T}$ (the trace of u_T on the torso surface) can be written $u_{T|\Gamma_T} = TF + C$, with C a constant such that $U = AF + C$, and T is a continuous operator $T = ([\text{Trace}] \circ A)$. To sum up, we minimize J over the space $\mathcal{E} = \big\{(U, F)\,|\,U \in AF + \mathbb{R},\, F \in H^1(\Gamma_H)/\mathbb{R}\big\}$.

3.2.2 Existence of a minimizer $(\bar{U}, \bar{F})$

First, let us recall some theorems from [3].

Theorem 3 *Assume that the function φ: $E \to (-\infty, +\infty]$ is convex and strongly lower semi-continuous (l.s.c) over the Banach space E, then it is l.s.c in the weak topology $\sigma(E, E^\star)$.*

Theorem 4 *Let E, F be Banach spaces and T a linear operator from E to F. If T is continuous in the strong topology, then T is continuous for the weak topology $\sigma(E, E^\star) \to \sigma(F, F^\star)$, and conversely.*

Step 1: Minimizing sequence The functional J is always positive. Thus its infimum $m = \inf_{\mathcal{E}} J(U, F)$ is also positive or null. From the definition of the infimum, there exists a minimizing sequence $(U_n, F_n) = ((\bar{u}_n, u_{n,T}, u_{n,B}), F_n) \in \mathcal{E}$ such that

$$J\left(U_n, F_n\right) \overset{n\to\infty}{\to} m.$$

Step 2: Exhibit weakly convergent subsequences Let $J_n = J(U_n, F_n)$ be a minimizing sequence. Then for any point $(\tilde{U}, \tilde{F})$ in the space $\mathcal{E}$, there exists a rank from which $J(\tilde{U}, \tilde{F})$ is an upper bound for the minimizing sequence J_n. In particular, from a certain rank, $J(0,0)$ is an upper bound for J_n:

$$0 \leq \underbrace{\frac{1}{2}\int_{\Gamma_T} |u_{n,T} - z_T|^2}_{\geq 0} + \frac{\varepsilon}{2}|F_n|^2_{H^1(\Gamma_H)} \leq J(0,0) = Cte. \tag{23}$$

In particular

- the sequence (F_n) is bounded in $H^1(\Gamma_H)$,
- the sequence $(u_{n,T|\Gamma_T})$ is bounded in $L^2(\Gamma_T)$.

We deduce the existence of a subsequence, again noted (F_n), that weakly converges to $\bar{F}$ in $H^1(\Gamma_H)$. The operator T being continuous from the Banach space $H^1(\Gamma_H)$ to the Banach space $H^{1/2}(\Gamma_T)$, it is weakly continuous (Theorem 4), and the subsequence TF_n weakly converges to $T\bar{F}$. Now using that $U_n = AF_n + C_n$, with (C_n) a sequence in $\mathbb{R}$, $u_{n,T|\Gamma_T} = AF_{n|\Gamma_T} + C_n$, and $AF_{n|\Gamma_T} = TF_n$ is bounded by continuity of T, we deduce that (C_n) is bounded in $\mathbb{R}$ and thus there exists a subsequence, again noted (C_n) that strongly converges to $\bar{C}$ in $\mathbb{R}$. Consequently, $U_n = AF_n + C_n \underset{n\to\infty}{\rightharpoonup} \bar{U} = A\bar{F} + \bar{C}$.

Step 3: Use of lower semi continuity The function $F \longmapsto |F|^2_{H^1(\Gamma_H)}$ is a convex continuous function. From Theorem 3, it is weakly lower semi continuous, so we can write the following inequality for the weak limit $\bar{F}$:

$$\frac{\varepsilon_1}{2}|\bar{F}|^2_{H^1(\Gamma_H)} \leq \liminf_{n\to\infty} \frac{\varepsilon_1}{2}|F_n|^2_{H^1(\Gamma_H)}.$$

Applying the same argument,

$$\frac{1}{2}\int_{\Gamma_T} \left|T\bar{F} + \bar{C} - z_T\right|^2 \leq \liminf_{n\to\infty} \frac{1}{2}\int_{\Gamma_T} |u_{nT} - z_T|^2 .$$

Finally,

$$J(\bar{U}, \bar{F}) \leq \liminf_{n\to\infty} J(U_n, F_n) = m,$$

so $J(\bar{U}, \bar{F}) = m$. We have exhibited a minimizer for J.

3.2.3 Uniqueness of the minimizer

We show that the Hessian of J is positive definite. Take (ϕ_U, ϕ_F) in the space $\mathcal{E}$ introduced in section 3.2.1:

$$\lim_{h\to 0^+} \frac{1}{h}\left[J(U + h\phi_U, F + h\phi_F) - J(U,F)\right] = \int_{\Gamma_T} (u_T - z_T)\phi_{u_T} + \varepsilon \int_{\Gamma_H} \partial_s F \partial_s \phi_F. \tag{24}$$

Thus

$$\begin{aligned} &\lim_{h\to 0^+} \frac{1}{h}\left[\langle \nabla J(U + h\phi_U, F + h\phi_F), (\phi_U, \phi_F)\rangle - \langle \nabla J(U,F), (\phi_U, \phi_F)\rangle\right] \\ &= \int_{\Gamma_T} \phi^2_{u_T} + \varepsilon \int_{\Gamma_H} (\partial_s \phi_F)^2 \geq 0. \end{aligned} \tag{25}$$

We must prove that this quantity is 0 only if the couple $(\phi_U, \phi_F) = (0,0)$. By definition, the H^1 semi-norm is a norm on the space $H^1(\Gamma_H)/\mathbb{R}$. So the term $\int_{\Gamma_H}(\partial_s\phi_F)^2$ is null only if $\phi_F = 0$. Concerning $\int_{\Gamma_T} \phi^2_{u_T}$, suppose that $\phi_F = 0$, then since $\phi_U = (\phi_{\bar{u}}, \phi_{u_T}, \phi_{u_B})$ satisfies (19), ϕ_U is constant ($= (C,C,C)$) on all three domains. Its trace on Γ_T is the same constant C, hence $\int_{\Gamma_T} \phi^2_{u_T}$ is 0 only if $C = 0$, that is $U = (0,0,0)$. The Hessian is thus positive definite, and J is strictly convex on the affine space $\mathcal{E}$.

3.3 Optimality conditions

We define the dual variables $\bar{\lambda}$, λ_T, λ_B in $H^1(\Gamma_H)$, $H^1(\Omega_T)$ and $H^1(\Omega_B)$, respectively. We define the Lagrangian function $\mathcal{L}(\bar{u}, u_T, u_B, \bar{\lambda}, \lambda_T, \lambda_B, F)$:

$$\begin{aligned}\mathcal{L}(\bar{u}, u_T, u_B, \bar{\lambda}, \lambda_T, \lambda_B, F) = &\frac{1}{2}\int_{\Gamma_T} |u_T - z_T|^2 + \frac{\varepsilon}{2}\int_{\Gamma_H} |\partial_s F|^2 \\ &+ \sigma_\ell h \int_{\Gamma_H} \partial_s \bar{u}\partial_s \bar{\lambda} + \frac{\sigma_{e,p}}{(1-\alpha)h}\int_{\Gamma_H} (\bar{u} - u_T)(\bar{\lambda} - \lambda_T) \\ &+ \frac{\sigma_{e,p}}{\alpha h}\int_{\Gamma_H} (\bar{u} - u_B)(\bar{\lambda} - \lambda_B) \\ &+ \sigma_T \int_{\Omega_T} \nabla u_T \cdot \nabla \lambda_T + \sigma_B \sigma_B \int_{\Omega_B} \nabla u_B \cdot \nabla \lambda_B - \int_{\Gamma_H} F\bar{\lambda}.\end{aligned} \tag{26}$$

The optimality condition system writes, for all $\bar{\lambda}$, λ_T, λ_B

$$0 = \left\langle \frac{\partial \mathcal{L}}{\partial \bar{u}}, \phi_{\bar{u}} \right\rangle = \sigma_\ell h \int_{\Gamma_H} \partial_s \phi_{\bar{u}} \partial_s \bar{\lambda} + \frac{\sigma_{e,p}}{(1-\alpha)h}\int_{\Gamma_H} \phi_{\bar{u}}(\bar{\lambda} - \lambda_T) + \frac{\sigma_{e,p}}{\alpha h}\int_{\Gamma_H} \phi_{\bar{u}}(\bar{\lambda} - \lambda_B), \tag{27}$$

$$0 = \left\langle \frac{\partial \mathcal{L}}{\partial u_T}, \phi_{u_T} \right\rangle = \int_{\Gamma_T} (u_T - z_T)\phi_{u_T} - \frac{\sigma_{e,p}}{(1-\alpha)h}\int_{\Gamma_H} \phi_{u_T}(\bar{\lambda} - \lambda_T) + \sigma_T \int_{\Omega_T} \nabla \phi_{u_T} \cdot \nabla \lambda_T, \tag{28}$$

$$0 = \left\langle \frac{\partial \mathcal{L}}{\partial u_B}, \phi_{u_B} \right\rangle = -\frac{\sigma_{e,p}}{\alpha h}\int_{\Gamma_H} \phi_{u_B}(\bar{\lambda} - \lambda_B) + \sigma_B \int_{\Omega_B} \nabla \phi_{u_B} \cdot \nabla \lambda_B, \tag{29}$$

$$\begin{aligned}0 = \left\langle \frac{\partial \mathcal{L}}{\partial \bar{\lambda}}, \phi_{\bar{\lambda}} \right\rangle = &\sigma_\ell h \int_{\Gamma_H} \partial_s \bar{u}\partial_s \phi_{\bar{\lambda}} + \frac{\sigma_{e,p}}{(1-\alpha)h}\int_{\Gamma_H} (\bar{u} - u_T)\phi_{\bar{\lambda}} + \frac{\sigma_{e,p}}{\alpha h}\int_{\Gamma_H} (\bar{u} - u_B)\phi_{\bar{\lambda}} \\ &- \int_{\Gamma_H} F\phi_{\bar{\lambda}},\end{aligned} \tag{30}$$

$$0 = \left\langle \frac{\partial \mathcal{L}}{\partial \lambda_T}, \phi_{\lambda_T} \right\rangle = -\frac{\sigma_{e,p}}{(1-\alpha)h}\int_{\Gamma_H} (\bar{u} - u_T)\phi_{\lambda_T} + \sigma_T \int_{\Omega_T} \nabla u_T \cdot \nabla \phi_{\lambda_T}, \tag{31}$$

$$0 = \left\langle \frac{\partial \mathcal{L}}{\partial \lambda_B}, \phi_{\lambda_B} \right\rangle = -\frac{\sigma_{e,p}}{\alpha h}\int_{\Gamma_H} (\bar{u} - u_B)\phi_{\lambda_B} + \sigma_B \int_{\Omega_B} \nabla u_B \cdot \nabla \phi_{\lambda_B}, \tag{32}$$

$$0 = \left\langle \frac{\partial \mathcal{L}}{\partial F}, \phi_F \right\rangle = \varepsilon \int_{\Gamma_H} F'\phi_F' - \int_{\Gamma_H} \phi_F \bar{\lambda}. \tag{33}$$

This is a linear system for the unknowns $\bar{u}, u_T, u_B, \bar{\lambda}, \lambda_T, \lambda_B$ which amounts to minimize the J functional on the functional space $\mathcal{E}$. Even if the system is large, it can be solved in one iteration as in [23]. The resolution of the inverse problem is thus very fast. Once the finite element matrix of the system is assembled, the LU factors of the matrix can be computed once and stored, and the solution of the inverse problem can be computed on a discrete set of times without recomputing the whole system. For instance, the activation maps reconstructed in section 4 were computed in less than 2 minutes on a standard 32 Go memory laptop with a Python code, without optimization. Note that we do not need to impose constraints on F or λ_T, such as a 0-mean constraint, or adjusting the constant on the potential to fit the data. Taking all elements in unconstrained H^1 space, those conditions arise naturally with the right test functions. For example, taking $(\phi_{\bar{\lambda}}, \phi_{\lambda_T}, \phi_{\lambda_B}) = (1, 1, 1)$, and inserting into the equations (30), (31), (32), we find $\int_{\Gamma_H} F = 0$.

3.4 Recovery of the average transmembrane potential

On a closed surface Γ_H, the control F is a second order derivative of the transmembrane voltage $\bar{v}$: $F = \sigma_{i,\ell}\partial_{ss}\bar{v}$ (see section 2.2.1). Thus, the average transmembrane voltage can be recovered up to a constant by solving the Neumann problem on Γ_H

$$\sigma_{i\ell} h \int_{\Gamma_H} \partial_s \bar{v}\partial_s \phi = -\int_{\Gamma_H} F\phi, \forall \phi \in H^1(\Gamma_H). \tag{34}$$

To ensure the invertibility of the system, we again add a small mass matrix on $\bar{v}$:

$$\sigma_{i\ell} h \int_{\Gamma_H} \partial_s \bar{v} \partial_s \phi + \varepsilon_1 \int_{\Gamma_H} \bar{v}\phi = -\int_{\Gamma_H} F\phi, \tag{35}$$

with ε_1 of order 10^{-14}. Then, the constant is adjusted by bounding below $\bar{v}$ by 0 on Γ_H to fit the Mitchell-Shaeffer model [22] during the activation process. It is of course not accurate when the transmembrane voltage is constant (on the plateau phase for example), however, we cannot obtain more information with a static resolution. A flat transmembrane signal produces a null extracardiac potential, thus an external knowledge on the temporal phase of the activation of the heart is necessary to discriminate an activation plateau from a rest phase.

4 Numerical results

4.1 Method

Numerical implementation As for the forward depth-averaged model (see section 2.3.1), we used P^1 Lagrange Finite Elements for solving the optimality condition system.

Regularization parameter for the Tikhonov regularization The regularization parameter was calibrated empirically on a few examples. In all noise free results presented below, we used $\varepsilon = 10^{-11}$.

Data construction As detailed in section 2.3.1, data are generated by several bidomain - Mitchell-Shaeffer model simulations. Only the activation of one heart beat was simulated (duration of approximately 50 ms). The potential u_T on the torso surface simulated with the bidomain model was extracted at several times to produce the data z_T of the inverse problem. Since the bidomain simulations and the optimal control problem do not share the same geometry (see section 2.3), the meshes for the bidomain simulations and the inverse problem are different. Though, the torso surface (exterior boundary of the domain) keeps the same geometry. Therefore, we project z_T, originally given on the bidomain mesh, on the inverse problem mesh through a cubic spline interpolation.

Note that neither the numerical discretization method (DDFV versus FEM), nor the geometry are the same between the forward bidomain simulations and the inverse optimal control resolution. Thus we completely avoid the inverse crime.

Quantities of interest We focus on the reconstruction of the activation times and study the ability of our inverse model to recover accurate activation maps. Therefore, we compare qualitatively the potentials $\bar{u}$ and voltages $\bar{v}$ reconstructed to the original bidomain potentials and voltages averaged in the heart. For instance, we expect the reconstructed extracellular potential to match the locations of strong derivatives with the reference. We also want the activated areas to be clearly identifiable on the reconstructed transmembrane voltage, by comparison with the resting areas.

We computed reference activation maps at the endocardium nodes and at the epicardium nodes for the four pacing protocols. The reference activation times were computed using the threshold method, that can be described as follows: considering that the transmembrane voltage v is normalized between 0 and 1 in the Mitchell-Shaeffer model, it consists in selecting, for each node of the mesh, the first time at which the transmembrane voltage v is above a threshold. That threshold is chosen here to be 0.6 to avoid the possible parasitic oscillations in the inverse solution $\bar{v}$ due to the L^2 regularization. Indeed, the activation maps are not significantly modified for thresholds taken between 0.4 and 0.6. We could also have used the $\min_t \frac{du}{dt}$ method (maxima in absolute value), also called the maximal deflexion method, that sees the activation time as the moment of minimal temporal slope of the potential u at a node. In that case, the derivative is computed with a centered Euler scheme. The two methods are equivalent for the bidomain reference signals, as shown in Figure 8. For the reconstructed signals, both methods are used, and studied. The corresponding activation maps are compared to the reference ones, qualitatively, and also quantitatively through the Correlation Coefficient (**CC**) indicator and the L^2 relative error (**L2err**). The Correlation Coefficient is simply the Pearson's correlation coefficient. Denoting by M_H, $\mathrm{AT}_{\mathbf{Ref}}$, and $\mathrm{AT}_{\mathbf{Thres}}$ the mass matrix over the heart layer, the reference activation map on $\bar{v}$, and the recovered activation maps with the threshold method respectively, the L^2 relative error writes

$$\mathbf{L2err} = \sqrt{\frac{\left(\mathrm{AT}_{\mathbf{Thres}} - \mathrm{AT}_{\mathbf{Ref}}\right)^T M_H \left(\mathrm{AT}_{\mathbf{Thres}} - \mathrm{AT}_{\mathbf{Ref}}\right)}{\mathrm{AT}_{\mathbf{Ref}}^T M_H \mathrm{AT}_{\mathbf{Ref}}}}.$$

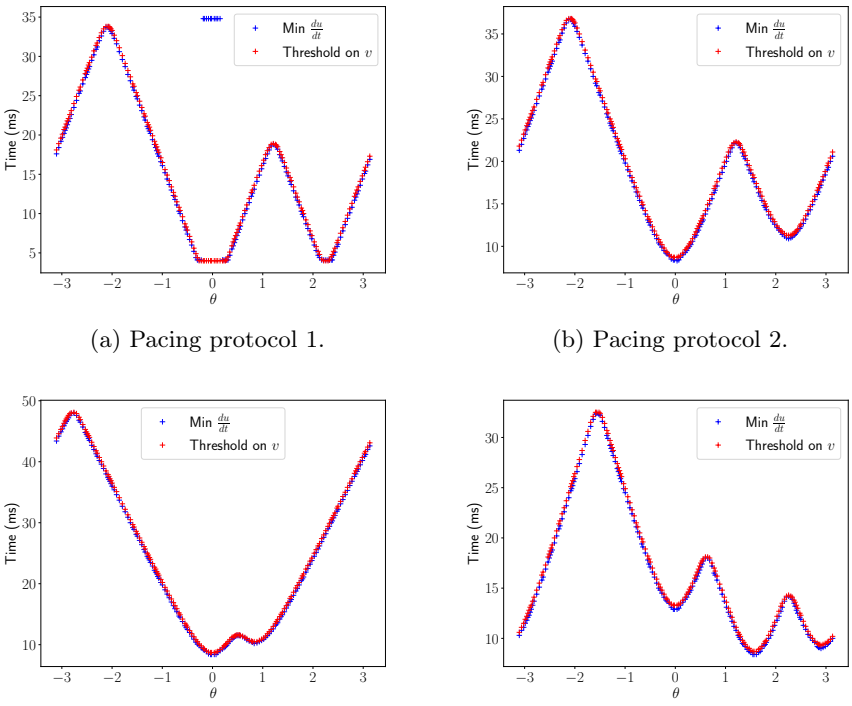

(a) Pacing protocol 1.

(b) Pacing protocol 2.

(c) Pacing protocol 3.

(d) Pacing protocol 4.

Figure 8: Activation maps of reference on the epicardium for the four pacing protocols, computed with the threshold method in red, and with the $\min_t \frac{du}{dt}$ method in blue. The two methods give equivalent activation maps.

The Pearson's correlation coefficient writes

$$\mathbf{CC} = \frac{\sum_{i=1}^{n}(\mathrm{AT}_{\mathbf{Thres}}[i] - \overline{\mathrm{AT}}_{\mathbf{Thres}})(\mathrm{AT}_{\mathbf{Ref}}[i] - \overline{\mathrm{AT}}_{\mathbf{Ref}})}{\sqrt{\sum_{i=1}^{n}(\mathrm{AT}_{\mathbf{Thres}}[i] - \overline{\mathrm{AT}}_{\mathbf{Thres}})^2}\sqrt{\sum_{i=1}^{n}(\mathrm{AT}_{\mathbf{Ref}}[i] - \overline{\mathrm{AT}}_{\mathbf{Ref}})^2}}.$$

The quantities $\overline{\mathrm{AT}}_{\mathbf{Thres\ /\ Ref}}$ are the average values of the samples: $\overline{\mathrm{AT}}_{\mathbf{Thres\ /\ Ref}} = \frac{1}{n}\sum_{i=1}^{n}\mathrm{AT}_{\mathbf{Thres}}[i]$, n being the number of samples (here the number of nodes on Γ_H), and i the node index.

4.2 Reconstructions at fixed time

In Figures 9 and 10, we present the one dimensional reconstructed potential $\bar{u}$ and voltage $\bar{v}$ on the heart layer Γ_H at two different moments of the activation process, for the four pacing protocols (see section 2.3.1). Figure 10 is taken after the epicardial breakthrough for all simulations. In that case, the activated parts of the heart are recognizable on the transmembrane voltage $\bar{v}$ reconstructed. Indeed, in this situation, the averaged signal over the thickness is representative of the volumic signal. Although parasitic oscillations are present on both reconstructed $\bar{u}$ and $\bar{v}$, those oscillations stay under the activation threshold. These oscillations are very typical of a L^2 type regularization term in the formulation of the optimization problem. On the contrary, before the epicardial breakthrough, as in Figure 9 for pacing protocols 2, 3 and 4, the reconstructed signals are of mediocre quality. It is more difficult to identify the activated parts of the heart. Indeed, in that case, the transmembrane voltage of reference significantly varies through the thickness of the heart (see the grey area between the endocardial and epicardial transmembrane voltages). Intrinsically, using averaged quantities masks part of the activation phenomenon, especially when the transmembrane voltage v is at rest on the epicardium while on the plateau phase on the endocardium. It is consistent to be unable to obtain good results in that case, especially in view of the performances of our forward depth-averaged model and of the intrinsic physics of the problem.

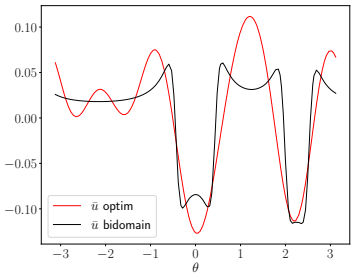

(a) Recovered $\bar{u}$ for pacing protocol 1.

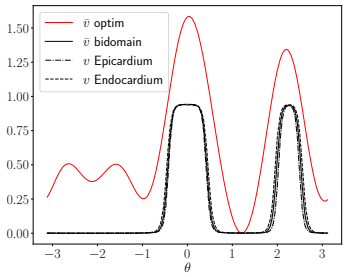

(b) Recovered $\bar{v}$ for pacing protocol 1.

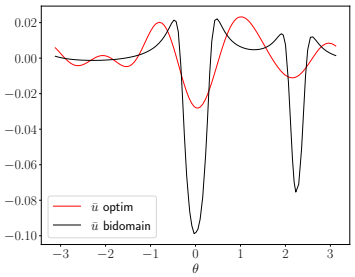

(c) Recovered $\bar{u}$ for pacing protocol 2.

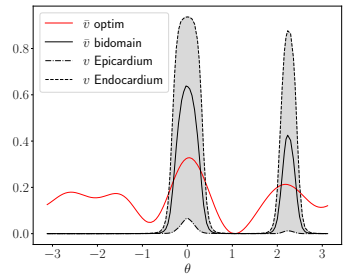

(d) Recovered $\bar{v}$ for pacing protocol 2.

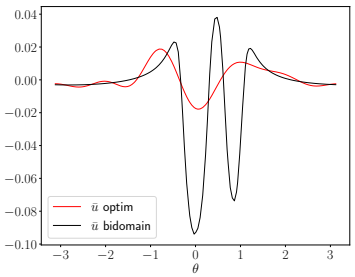

(e) Recovered $\bar{u}$ for pacing protocol 3.

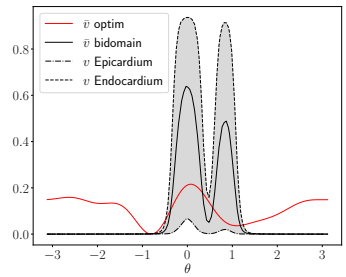

(f) Recovered $\bar{v}$ for pacing protocol 3.

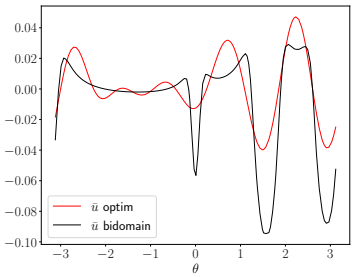

(g) Recovered $\bar{u}$ for pacing protocol 4.

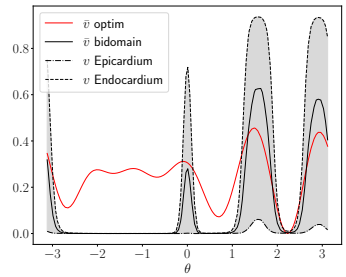

(h) Recovered $\bar{v}$ for pacing protocol 4.

Figure 9: Examples of recovered solutions $\bar{u}$ (left) and $\bar{v}$ (right) on the heart for the four pacing protocols at time 6 ms. The angle θ is a coordinate for the heart points. The red line represents the reconstructed solution, and the black line the bidomain reference. The dash-dotted and dashed lines represent the transmembrane voltage v of reference on the epicardium and endocardium respectively. The grey area underlines the variability of the transmembrane voltage in the depth of the heart. The regularization parameter ε is empirically chosen at 10^{-11}. Note that at the beginning of the activation phase, the activation of the endocardium is not visible on the torso signal.

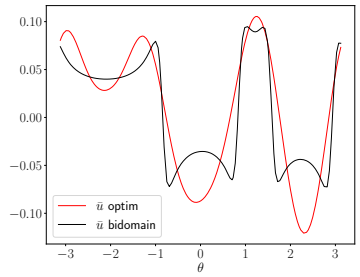

(a) Recovered $\bar{u}$ for pacing protocol 1.

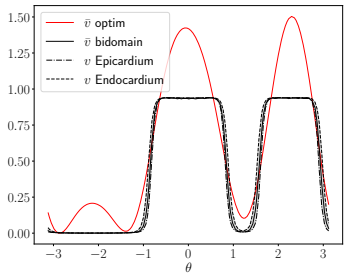

(b) Recovered $\bar{v}$ for pacing protocol 1.

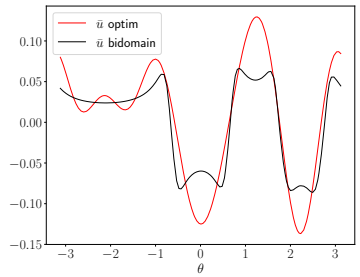

(c) Recovered $\bar{u}$ for pacing protocol 2.

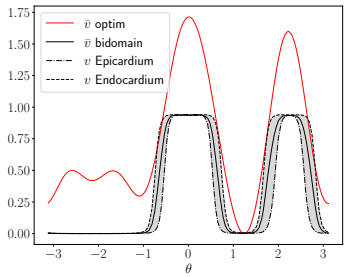

(d) Recovered $\bar{v}$ for pacing protocol 2.

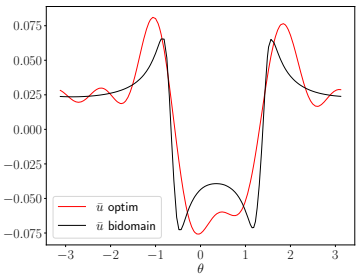

(e) Recovered $\bar{u}$ for pacing protocol 3.

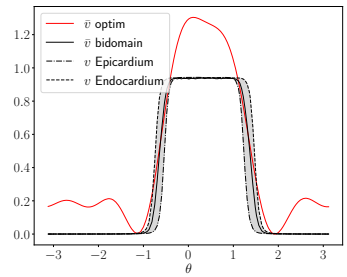

(f) Recovered $\bar{v}$ for pacing protocol 3.

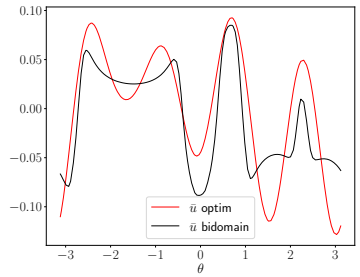

(g) Recovered $\bar{u}$ for pacing protocol 4.

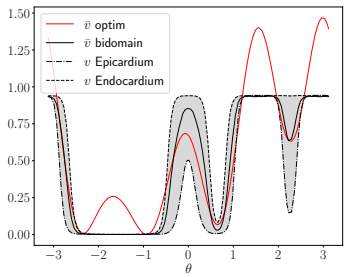

(h) Recovered $\bar{v}$ for pacing protocol 4.

Figure 10: Examples of recovered solutions $\bar{u}$ (left) and $\bar{v}$ (right) on the heart for the four pacing protocols at time 13 ms. The angle θ is a coordinate for the heart points. The red line represents the reconstructed solution, and the black line the bidomain reference. The dash-dotted and dashed lines represent the transmembrane voltage v of reference on the epicardium and endocardium respectively. The grey area underlines the variability of the transmembrane voltage in the depth of the heart. The regularization parameter ε is empirically chosen at 10^{-11}.

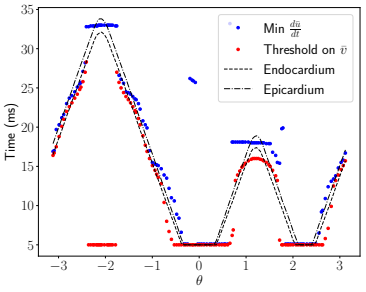

(a) Pacing protocol 1: reconstructed activation map.

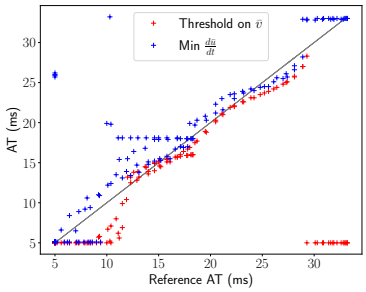

(b) Pacing protocol 1: correlations.

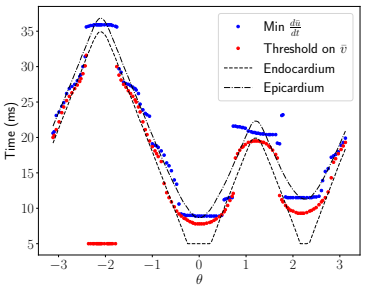

(c) Pacing protocol 2: reconstructed activation map.

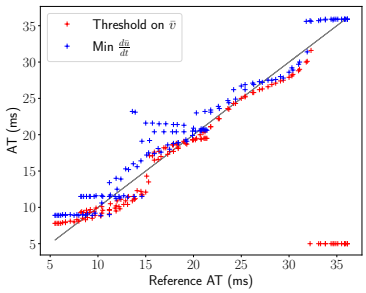

(d) Pacing protocol 2: correlations

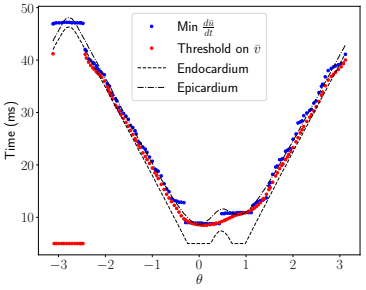

(e) Pacing protocol 3: reconstructed activation map.

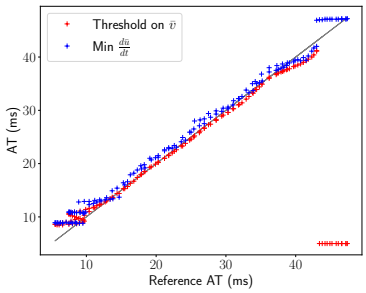

(f) Pacing protocol 3: correlations

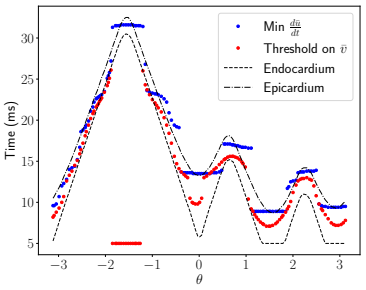

(g) Pacing protocol 4: reconstructed activation map.

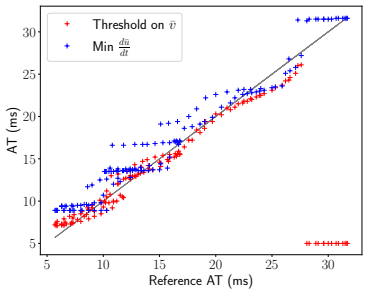

(h) Pacing protocol 4: correlations

Figure 11: Average activation times in the thickness for the four pacing protocols from top to bottom. On the left figures, the black curves represent the reference activation maps on the endocardium (dashed) and on the epicardium (dash-dotted). The blue dots indicate the activation times computed with the $\min_t \frac{du}{dt}$ method applied on the recovered potential $\bar{u}$, while the red dots are the activation times computed with the threshold method on the recovered $\bar{v}$. The figures on the right represent the reconstructed activation times of both methods as a function of the reference average activation times in the thickness of the myocardium wall.

4.3 Activation map recovery

In Figure 11, we show the reconstructed activation maps computed with the two methods described in Section 4.1. To visualize the correlation between the true and recovered activation maps, we also plotted the recovered activation maps as a function of the reference average activation times (threshold method applied on $\bar{v}$ from the bidomain simulation). In the four pacing protocols cases, the $\min_t \frac{du}{dt}$ method presents artificial lines of block, that are absent with the threshold method. Those lines of blocks have already been identified as an issue in several articles [28], [5], and complex algorithms have been developed to smoothen reconstructed activation maps in ECGi. Our reconstructions suggest that using the transmembrane voltage associated with the threshold method to compute activation maps allows to avoid those artefacts and recover smoother and more accurate maps.

In order to measure quantitatively the accuracy of the recovered activation maps with the threshold method, we use the **CC** and **L2err** indicators. On Figure 11, some outliers values are visible at the end of the activation process. We eliminate those values in order to assess the recovery of the activation sequence before a certain time limit called (**AT lim**): specifically, we truncate the activation maps to ignore the points of the heart which reference activation time is superior to **AT lim** above which the reconstructed activation time is stuck at 0 on the Figure. Then, we compute the Correlation Coefficient (**CC**) between the reference activation times on $\bar{v}$ and the recovered activation times from the threshold method. We also compute the L^2 relative error (**L2err**) on the heart surface between those two activation maps. These indicators are presented in Table 1. For the four stimulation protocols, the L^2 relative error of the recovered truncated maps is less than 12%, and the correlation coefficient with the reference map is above 0.98. Overall, for the four protocols, our method is able to reconstruct activation maps that are

Pacing protocol	1	2	3	4
AT lim (ms)	29	30	41	26.5
CC	0.98	0.98	0.99	0.99
L2err	0.12	0.08	0.05	0.06

Table 1: Correlation coefficients and L^2 relative errors obtained on the truncated recovered activation maps for the four different protocols. We truncated the activation times values above **AT lim**.

bounded between by the reference values on the endocardium and the epicardium, and that have a high correlation with the true activation maps. The protocol 3 leads to substantially better results than the other protocols. Its activation sequence almost behaves as if there were only one stimulation point, thus following a simpler pattern, easier to recover. We however notice than we cannot distinguish the two initial activation points.

The threshold method also presents some drawbacks. The activation times (ATs) reconstructed seem to jump sometimes from epicardium ATs to endocardium ATs. This is probably an effect of the averaging process, as explained before. Again, the phenomena on the endocardium are very difficult to observe. Moreover, at the very end of the activation sequence (after **AT lim**), our method is not able to identify activation times. As a matter of fact, the average transmembrane potential $\bar{v}$ is reconstructed up to a constant, that we fix by imposing $\min_\theta \bar{v} = 0$. Thus, when the plateau phase is reached for almost all points of the heart (constant $\bar{v} \approx 1$ for all θ), the global amplitude of the signal decreases. The minima being still fixed at 0, the reconstructed transmembrane voltage simply appears to fall back to 0 on the whole heart. Nevertheless, we believe that mixing information from the threshold method and from the maximal deflection method would help to identify the end of the activation process and easily replace the final activation times by activation times computed with the maximal deflection method.

4.4 Gaussian noise perturbation

The robustness of the inverse model is evaluated by adding a Gaussian noise to the simulated data. The noise follows a normal law of 0-mean and standard deviation of 1 that is multiplied by some percentage of the amplitude of the data z_T. We make 50 trials of activation map recovery for all test cases, and plot the median activation times recovered, as well as their standard deviation over the 50 trials. Preliminary tests on the method for computing activation times and on the role of the regularization parameter were carried out on protocol 3, for which we obtained the best noise-free activation map reconstructions.

Concerning the method for the activation map recovery, there is a clear advantage in using the threshold method for noisy data. Indeed, by differentiating the reconstructed signal, the $\min_t \frac{du}{dt}$ method

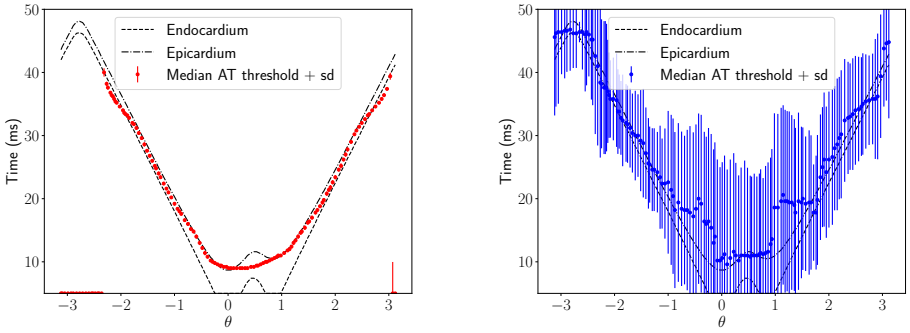

(a) Activation map recovered with the threshold method.

(b) Activation map recovered with the $\min_t \frac{du}{dt}$ method.

Figure 12: Comparison between the two activation map reconstruction methods, with a 4% Gaussian noise on the data, and a regularization parameter $\varepsilon = 10^{-9}$ on 50 trials. On the left, the threshold method was used, while on the right, we used the $\min_t \frac{du}{dt}$ method. The vertical lines represent the standard deviation, and the dots represent the median activation time over the 50 trials. The black dash-dotted and dashed lines represent the true activation maps on the endocardium and epicardium respectively.

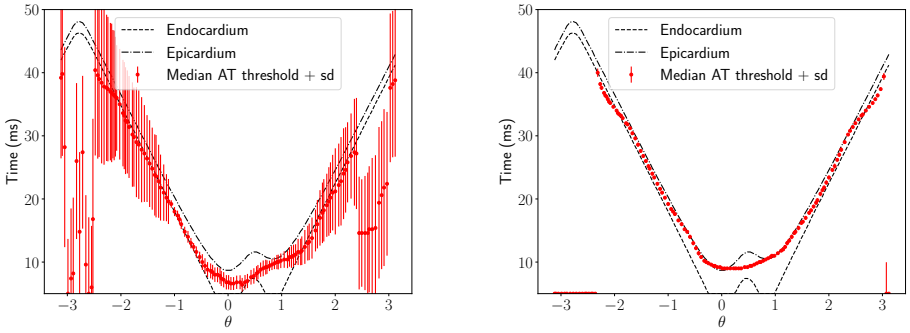

(a) 4% noise on the data. Parameter $\varepsilon = 10^{-11}$.

(b) 4% noise on the data. Parameter $\varepsilon = 10^{-9}$.

Figure 13: Degradation of the recovered signal with noise, and stability through regularization for the protocol 3. All activation maps are now computed with the threshold method. The red dots represent the median activation time found by the threshold method, over the 50 trials. The vertical lines represent the standard deviation over the 50 trials. The black dash-dotted and dashed lines represent the true activation maps on the endocardium and epicardium respectively.

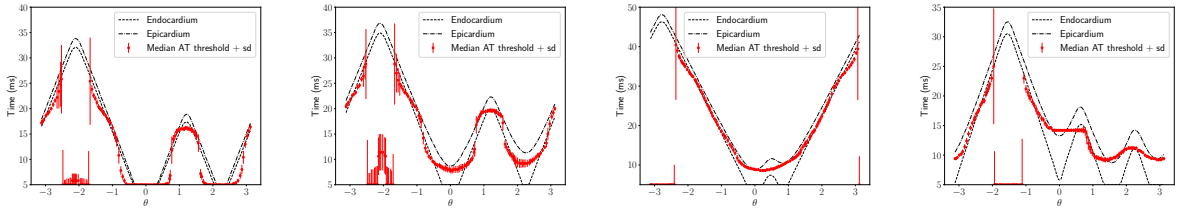

(a) Pacing protocol 1. (b) Pacing protocol 2. (c) Pacing protocol 3. (d) Pacing protocol 4.

Figure 14: Recovered activation maps with 10% noise on the 50 trials for the activation patterns 1, 2, 3 and 4. Parameter ε is fixed at 10^{-9}. The red dots represent the median activation time found by the threshold method, over the 50 trials. The red vertical lines represent the standard deviation over the 50 trials. The black dash-dotted and dashed lines represent the true activation maps on the endocardium and epicardium respectively.

becomes extremely unstable in presence of noise. In comparison, with the same regularization parameter, the threshold method allows to obtain more stable activation maps (see Figure 12).

As shown in Figures 13 and 14, the more noise in the data (4% for Figure 13 and 10% for subfigure (14c)), the more the recovered signals and activation maps are degraded. As illustrated in Figure 13, in order to ensure stability, the regularization parameter ε must be increased. In Figures 13 and 14, the increase by two orders of magnitude in the regularization parameter (from 10^{-11} to 10^{-9}) allows to stabilize the activation maps recovered for the 50 trials. In Figure 14, activation maps for the four patterns are reconstructed with a 10% noise on the torso data. The quality of the activation maps is deteriorated in comparison with the absence of noise, and, for the pattern 3, with a 4% noise, however, the activation maps remain correct.

4.5 Standard conductivity estimations

In clinical cases, the exact conductivities in the heart, torso, and blood are not known. The conductivity tensors σ_i, σ_e, and $\sigma_{T/B}$ are often supposed isotropic or proportional, especially when using surface source models [9, 32]. However, the differences in the conductivity tensors in the models can significantly change the solutions. Hence, to be applicable in practice, our inverse model must be able to reconstruct accurate activation maps even with a priori isotropic conductivity estimations.

In this part, the conductivities chosen for the depth-averaged model are deliberately different from the ones used in the bidomain simulations. In the bidomain simulation, the (scaled) conductivities were taken as: $\sigma_{i,\ell} = 1.741$, $\sigma_{i,p} = 0.1934$, $\sigma_{e,\ell} = 3.906$, $\sigma_{i,p} = 1.970$ and $\sigma_T = \sigma_B = 2$. In the depth-averaged model, all conductivities are chosen equal to 1, a simple arbitrary value located in-between the minimimal and maximal bidomain conductivities. Using the generated data from the four bidomain pacing protocols, the activation maps are reconstructed with the isotropic depth-averaged model. Figure 15 presents the reconstructed maps for that case.

Surprisingly, the recovered activation maps calculated with the threshold method in Figure 15 are very faithful to the activation maps of the epicardium only. We also tested with all conductivities equal to 3, and obtained maps that were bounded between by the true values of activation times on the epicardium and endocardium, still with greater resemblance to the epicardial map. It seems that the less precise we are on the conductivity coefficients, the closer we get to the epicardial activation map. Indeed, epicardial signals are more visible on the torso surface than signals from within the myocardial volume. They produce more important variations in the body surface signal.

5 Conclusion and discussion

The proposed model allows to enrich the classical resolution of the inverse problem of electrocardiography on the epicardium only, while retaining its simplicity. It incorporates information on the myocardial volume and enables the reconstruction of the average transmembrane voltage over the myocardial thickness.

Our results on activation maps show the method's ability to recover activation maps delimited by activation time values on the epicardium and endocardium. We are able to shed light on the underlying activation process in the myocardial volume. Combined with a fast resolution of the classical epicardial model, this approach holds great promise for gaining further insight into transmural activity. Anyway, this work constitutes a preliminary study, based on simplifying assumptions concerning a 2D heart geometry. Future work should therefore focus on integrating the particularities of realistic 3D geometries, and of a non-constant depth h.

We also highlight the need to reconstruct the transmembrane voltage v, to recover activation maps. The combination with the threshold method for calculating activation times appears to produce activation maps that are more reliable and less sensitive to noise than the maximum deflection method. In particular, the method is less likely to produce artificial lines of block. We will continue to investigate activation map reconstruction methods in future work.

6 Acknowledgments

This study received financial support from the French Government as part of the "Investments of the Future" program managed by the National Research Agency (ANR), Grant reference ANR-10-IAHU-04. This work was also funded by a MITACS-Inria Globalink Research Award, for the first author to spend

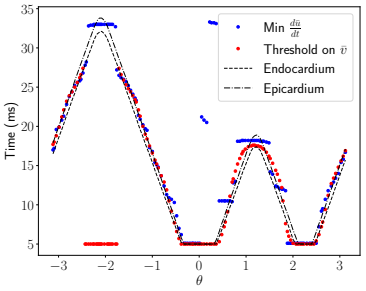

(a) Pacing protocol 1: reconstructed activation map.

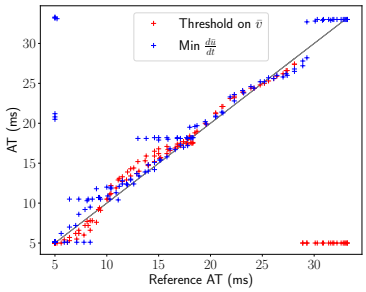

(b) Pacing protocol 1: correlations.

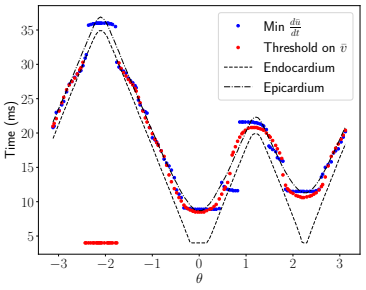

(c) Pacing protocol 2: reconstructed activation map.

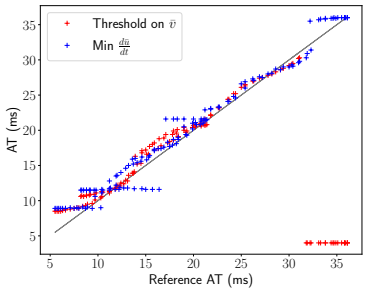

(d) Pacing protocol 2: correlations

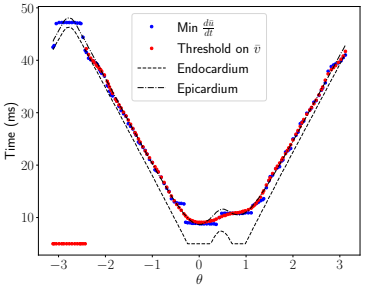

(e) Pacing protocol 3: reconstructed activation map.

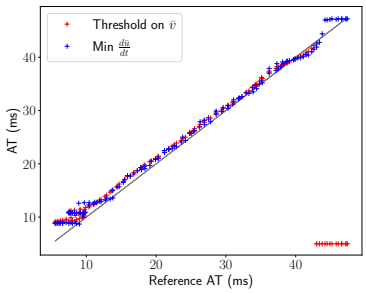

(f) Pacing protocol 3: correlations

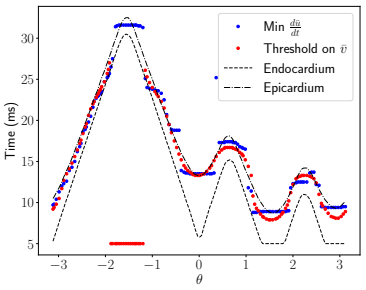

(g) Pacing protocol 4: reconstructed activation map.

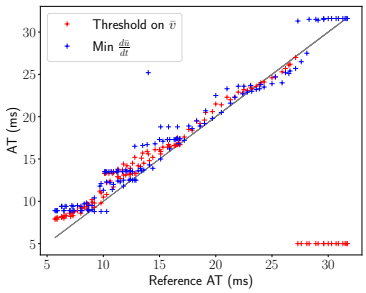

(h) Pacing protocol 4: correlations

Figure 15: Average activation maps reconstructed in the thickness with isotropic conductivity assumptions for the four pacing protocols from top to bottom. The black dash-dotted and dashed curves represent the reference activation map from the bidomain simulation computed on the endocardium and epicardium with the threshold method. The red dots represent the average activation map in the thickness recovered with the threshold method. The blue dot represents the map reconstructed with the $\min_t \frac{du}{dt}$ method.

four months at the University of Ottawa, and a Discovery Grant (no. RGPIN-2019-06855) of the Natural Sciences and Engineering Research Council (NSERC) to the second author.

References

[1] Laura Bear et al. "Introduction to noninvasive cardiac mapping". In: *Cardiac electrophysiology clinics* 7.1 (2015), pp. 1–16.

[2] Faker Ben Belgacem. "Why is the Cauchy problem severely ill-posed?" In: *Inverse problems* 23.2 (2007), p. 823.

[3] Haim Brezis and Haim Brézis. *Functional analysis, Sobolev spaces and partial differential equations*. Vol. 2. 3. Springer, 2011.

[4] Ruben Doste et al. "A rule-based method to model myocardial fiber orientation in cardiac biventricular geometries with outflow tracts". In: *International journal for numerical methods in biomedical engineering* 35.4 (2019), e3185.

[5] Josselin Duchateau, Mark Potse, and Remi Dubois. "Spatially coherent activation maps for electrocardiographic imaging". In: *IEEE Transactions on Biomedical Engineering* 64.5 (2016), pp. 1149–1156.

[6] Josselin Duchateau et al. "Performance and limitations of noninvasive cardiac activation mapping". In: *Heart rhythm* 16.3 (2019), pp. 435–442.

[7] Jean-Philippe Empana et al. "Incidence of Sudden Cardiac Death in the European Union". In: *Journal of the American College of Cardiology* 79.18 (2022), pp. 1818–1827. DOI: 10.1016/j.jacc.2022.02.041. eprint: https://www.jacc.org/doi/pdf/10.1016/j.jacc.2022.02.041. URL: https://www.jacc.org/doi/abs/10.1016/j.jacc.2022.02.041.

[8] Marc Ethier and Yves Bourgault. "Semi-implicit time-discretization schemes for the bidomain model". In: *SIAM Journal on Numerical Analysis* 46.5 (2008), pp. 2443–2468.

[9] David B Geselowitz. "Description of cardiac sources in anisotropic cardiac muscle: application of bidomain model". In: *Journal of electrocardiology* 25 (1992), pp. 65–67.

[10] David B Geselowitz and WT Miller. "A bidomain model for anisotropic cardiac muscle". In: *Annals of biomedical engineering* 11 (1983), pp. 191–206.

[11] Bin He, Guanglin Li, and Xin Zhang. "Noninvasive imaging of cardiac transmembrane potentials within three-dimensional myocardium by means of a realistic geometry anisotropic heart model". In: *IEEE Transactions on Biomedical Engineering* 50.10 (2003), pp. 1190–1202.

[12] Clément Jourdana and Paola Pietra. "An interface formulation for the Poisson equation in the presence of a semiconducting single-layer material". In: *arXiv preprint arXiv:2301.13483* (2023).

[13] Alexander Kalinin, Danila Potyagaylo, and Vitaly Kalinin. "Solving the inverse problem of electrocardiography on the endocardium using a single layer source". In: *Frontiers in physiology* (2019), p. 58.

[14] Vitaly Kalinin, Alexander Shlapunov, and Konstantin Ushenin. "On uniqueness theorems for the inverse problem of electrocardiography in the Sobolev spaces". In: *ZAMM-Journal of Applied Mathematics and Mechanics/Zeitschrift für Angewandte Mathematik und Mechanik* 103.1 (2023), e202100217.

[15] Vitaly Kalinin et al. "On the correctness of the transmembrane potential based inverse problem of ECG". In: *2017 Computing in Cardiology (CinC)*. IEEE. 2017, pp. 1–4.

[16] Markus Köppel et al. "A Lagrange multiplier method for a discrete fracture model for flow in porous media". In: *Computational Geosciences* 23 (2019), pp. 239–253.

[17] Glenn Terje Lines, Per Grottum, and Aslak Tveito. "Modeling the electrical activity of the heart: a bidomain model of the ventricles embedded in a torso". In: *Computing and Visualization in Science* 5 (2003), pp. 195–213.

[18] GT Lines et al. "Mathematical models and numerical methods for the forward problem in cardiac electrophysiology". In: *Computing and Visualization in Science* 5 (2003), pp. 215–239.

[19] Alejandro Lopez-Rincon, Mostafa Bendahmane, and Bedr'Eddine Ainseba. "On 3D numerical inverse problems for the bidomain model in electrocardiology". In: *Computers & Mathematics with Applications* 69.4 (2015), pp. 255–274.

[20] Vincent Martin, Jérôme Jaffré, and Jean E Roberts. "Modeling fractures and barriers as interfaces for flow in porous media". In: *SIAM Journal on Scientific Computing* 26.5 (2005), pp. 1667–1691.

[21] Bernd Messnarz et al. "A new spatiotemporal regularization approach for reconstruction of cardiac transmembrane potential patterns". In: *IEEE transactions on Biomedical Engineering* 51.2 (2004), pp. 273–281.

[22] Colleen C Mitchell and David G Schaeffer. "A two-current model for the dynamics of cardiac membrane". In: *Bulletin of mathematical biology* 65.5 (2003), pp. 767–793.

[23] Bjørn Fredrik Nielsen, Xing Cai, and Marius Lysaker. "On the possibility for computing the transmembrane potential in the heart with a one shot method: An inverse problem". In: *Mathematical Biosciences* 210.2 (2007), pp. 523–553.

[24] World Health Organization. URL: `https://www.who.int/news-room/fact-sheets/detail/cardiovascular-diseases-(cvds)`.

[25] Andrew J Pullan et al. "The inverse problem of electrocardiography". In: *Comprehensive electrocardiology* 1 (2010), pp. 299–344.

[26] Gwladys Ravon et al. "A parameter optimization to solve the inverse problem in electrocardiography". In: *International Conference on Functional Imaging and Modeling of the Heart*. Springer. 2017, pp. 219–229.

[27] Miriam Rioux and Yves Bourgault. "A predictive method allowing the use of a single ionic model in numerical cardiac electrophysiology". In: *ESAIM: Mathematical Modelling and Numerical Analysis* 47.4 (2013), pp. 987–1016.

[28] Steffen Schuler et al. "Reducing line-of-block artifacts in cardiac activation maps estimated using ECG imaging: A comparison of source models and estimation methods". In: *IEEE Transactions on Biomedical Engineering* 69.6 (2021), pp. 2041–2052.

[29] Neil T Srinivasan and Richard Schilling. "Sudden Cardiac Death and Arrhythmias". In: *Arrhythmia & Electrophysiology Review 2018;7(2):111–7.* (2018). DOI: `10.15420/aer.2018:15:2`. URL: `https://doi.org/10.15420/aer.2018:15:2`.

[30] Leslie Tung. "A bi-domain model for describing ischemic myocardial dc potentials." PhD thesis. Massachusetts Institute of Technology, 1978.

[31] Peter M Van Dam et al. "Non-invasive imaging of cardiac activation and recovery". In: *Annals of biomedical engineering* 37 (2009), pp. 1739–1756.

[32] Jeanne van der Waal et al. "In silico validation of electrocardiographic imaging to reconstruct the endocardial and epicardial repolarization pattern using the equivalent dipole layer source model". In: *Medical & biological engineering & computing* 58 (2020), pp. 1739–1749.

[33] Linwei Wang et al. "Physiological-model-constrained noninvasive reconstruction of volumetric myocardial transmembrane potentials". In: *IEEE Transactions on Biomedical Engineering* 57.2 (2009), pp. 296–315.